The '4D-Earth-Swarm' project: CCN1

Imaging the deep Earth from rapid geomagnetic field changes

Draft Scientific Report (MS2)

a project supported by ESA

September 2023

list of partners:

- ISTerre, Grenoble, France (PI)
- ROB, Brussels, Belgium
- Univ. of Leeds, UK
- IPG, Paris, France
- DTU Space, Copenhagen, Denmark

Contents

J. AUBERT
IPG PARIS

Chapter 1

Introduction to CCN1

Nicolas Gillet, together with the 4D-Earth consortium

The objective of the main contract to understand the rapid (interannual) changes in the geomagnetic field was successfully achieved by the contractor by providing a general framework with use of Swarm observations that enables their physical understanding. This also led to the detection of Magneto-Coriolis (MC) waves for the first time. This dynamics explains sudden changes in the rate of change of the geomagnetic field (a.k.a 'jerks'), associated with pulses in the second time derivative of the field. The overarching goal of CCN1 is to contribute to a better understanding of these dynamics and to map the base state within Earth's outer core, on top of which Quasi-Geostrophic (QG) hydro-magnetic modes exist. Knowledge of the basic state within the core is expected to advance our understanding of the processes in the core generating and maintaining the Earth's dynamo. In addition, a first model of the laterally varying electrical conductivity in the region above the Core Mantle Boundary (CMB) shall be produced, using a bottom-up approach where the core dynamics is used as a source to sample the mantle conductivity. The relation between such lateral variations and the Large Low-Shear-Velocity Provinces (LLSVP) will be discussed. It should contribute to improving our understanding of the dynamical and thermo-chemical balances within the deep Earth, and thus lead to better constrain geodynamical models.

Motivations for the CCN

Sudden changes in the rate of change of the geomagnetic field (or 'jerks', see Mandea et al, 2010, for a review) have been first detected some 50 years ago in ground-based records. Over the satellite era they have been associated with pulses in the second time derivative of the field or 'secular acceleration' (Chulliat and Maus, 2014; Finlay et al, 2016). These dynamics have largely remained unexplained so far.

Prior to our project kick-off, acceleration pulses resembling those observed in geomagnetic time series had only recently been identified in geodynamo simulations approaching Earth conditions (Aubert and Finlay, 2019), thanks to a parameterization of turbulent processes (Large Eddy Simulations, or LES, see Aubert et al, 2017). They were at that stage associated in computations with one family of

quasi-geostrophic (QG, or axially invariant due to the domination of the Coriolis force) motions, non-axisymmetric QG Alfvén waves, in which inertia balances the Lorentz force in the momentum balance.

The work carried out by our consortium has allowed us to design a general framework that provides a physical understanding of rapid geomagnetic field changes. It also led to the first detection of Magneto-Coriolis (MC) waves (see Fig. 1.1) thanks to two decades of continuous magnetic monitoring from space, most recently via the Swarm mission (see Hammer et al, 2021; Finlay et al, 2020). As described below, our research domain has thus significantly evolved over the past two years.

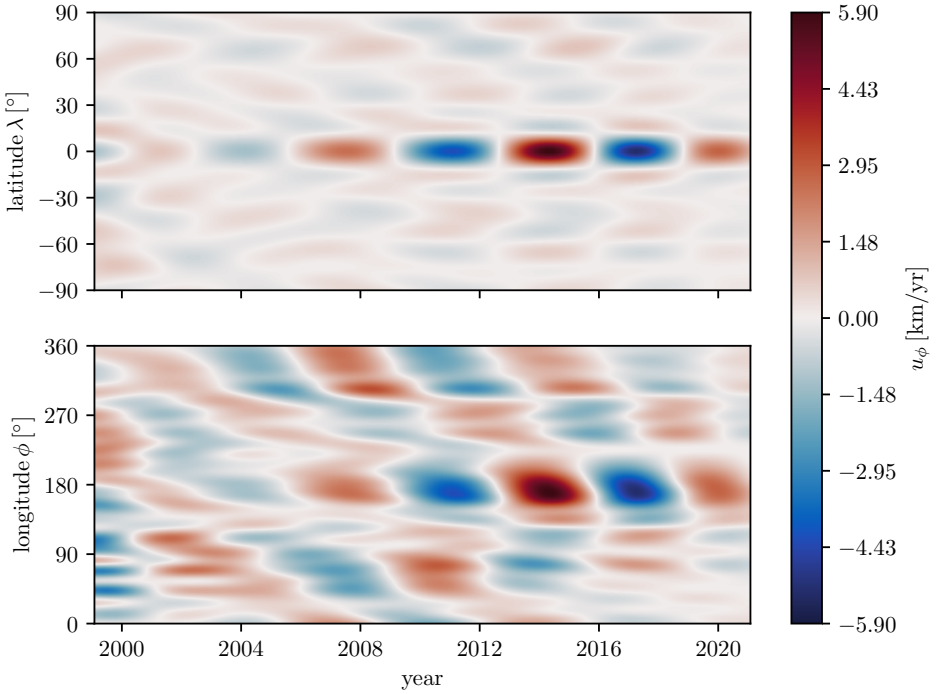

Figure 1.1: QG MC modes of period $T \sim 7$ years, detected from geomagnetic satellite data (Gillet et al, 2022). The time-latitude map for the core surface azimuthal velocity at longitude 180°E (top) shows several zero-crossings in latitude and a stronger signature towards the equator. The time-longitude diagram at the equator (bottom) illustrates a westward phase velocity of the mode, with a speed about 1500 km/yr.

First, the '71%-path' dynamo simulation run at extreme parameters (Aubert and Gillet, 2021) have shown many occurrences of magnetic acceleration events (see the catalog provided with Task E). These may be characterized depending on the relative importance of advection by the flow and wave propagation (Aubert et al, 2022). The catalog is rich in events, and a detailed analysis is required in order

to assess whether all rapid changes computed so far share the same observational and dynamical properties, and how they compare with those recorded from ground or space. The 71%-path simulation also shows QG hydromagnetic waves triggered in an ubiquitous manner, whether it be torsional (axisymmetric) Alfvén waves and QG Alfven waves on period about the Alfvén time (equivalent to $\sim$ 2 yrs in the core), or Rossby waves on shorter periods.

Meanwhile, an important breakthrough from our consortium has been the discovery of QG MC waves with interannual periods. On the large length-scales that are accessible with magnetic records ($\sim$ 800 km at the core surface), MC waves were previously believed to occur on centennial and longer periods (Hide, 1966). However, the eigenmode study by Gerick et al (2021) shows that QG MC modes do also exist on interannual periods, with a magnetic signature strongest close to the equator, as observed in satellite magnetic data (Finlay et al, 2020). This study constitutes an important theoretical and computational achievement, where two dimensional velocity perturbations in a sphere have been for the first time coupled with three-dimensional magnetic perturbations satisfying a potential field condition at the core surface.

We succeeded in detecting such a QG MC mode, with period $\sim$ 7 yr, in core surface flows inverted from satellite magnetic data (Gillet et al, 2022). These present stronger patterns in the equatorial belt (of amplitude up to 5 km/yr), and travel westward at the equator, at a phase speed $\sim$ 1500 km/yr much larger than the fluid velocity (see Fig. 1.1). This revised understanding of rapid core dynamics paves the way to a deterministic modelling of subdecadal geomagnetic field changes; a crucial part of this framework is knowledge of magnetic field within the outer core. It is the overarching goal of the current CCN to map the base state within the Earth's outer core, on top of which QG hydro-magnetic modes exist. Knowledge of the basic state withing the core will advance our understanding of the processes in the core generating and maintaining the Earth's dynamo.

So far, the main information on the field deep in the core has been obtained through the detection of torsional Alfvén waves in magnetic observations (Gillet et al, 2010). This knowledge is however restricted to a one dimensional profile, the r.m.s. of the cylindrical radial field B_s averaged over φ and z as a function of the distance s to the rotation axis (with (s, φ, z) the cylindrical coordinates). In principle, the detected QG MC modes will give access to a two dimensional map of the z-averaged r.m.s. B_s (as a function of s and φ). To more fully understand these exciting new modes and the constrains they provide we need to explore further their sensitivity to the background field with dedicated direct numerical simulations and eigenmodes studies. Furthermore, a deeper understanding of the magnetic boundary conditions relevant for the interannual dynamics may lead to improved spatial constraints on the core flow recovery. Of course, not all the magnetic signal recorded by Swarm is attached to such modes; unresolved processes also account for a significant fraction of interannual field changes (about one half according to our recent work). These two sources of signal are covariant, and properly accounting for the interplay between QG MC modes and subgrid-scale processes should

allow us to reduce uncertainties on core flows, and thus enhance the recovery of the field deep in the core.

In this quest to use Swarm observations of sub-decadal core field variations to obtain the magnetic magnetic field and fluid flow within the core, we plan to address the several issues listed below:

- upgrade and extend the geomagnetic datasets, in a manner that is suited for incorporation into core dynamics analysis tools, including adapted information on data error covariances (Task L);
- improve the `pygeodyn` core flow re-analysis tool used to isolate QG MC waves from observations, so that it better handles unresolved processes and their relation with large length-scale flows, aiming to reduce uncertainties (Task M);
- systematically detect and characterize jerks in satellite, ground observatory and geodynamo simulation data (Task N);
- image the basic state (magnetic field, velocity field and buoyancy field) within the outer core from Swarm data products, in a framework that incorporates both the statistical and dynamical information from geodynamo simulations (Task O);
- document the sensitivity of QG MC modes to the background magnetic field with an eigenmodes solver (Task P);
- extract geophysical knowledge on the core magnetic field and the lower mantle conductance in the equatorial region of the Earth's core, from the analysis of QG MC modes detected in core flow models (Task Q);
- characterize the propagation of QG MC and QG Alfvén waves in forward 3D simulations, together with the magnetic boundary conditions they satisfy, and document how these could be considered to improve the constraint on core surface flow models (Task R).

Bibliography

Aubert J, Finlay CC (2019) Geomagnetic jerks and rapid hydromagnetic waves focusing at Earth's core surface. Nature Geosci 12(5):393–398, DOI 10.1038/s41561-019-0355-1

Aubert J, Gillet N (2021) The interplay of fast waves and slow convection in geodynamo simulations nearing earth's core conditions. Geophys J Int DOI https://doi.org/10.1093/gji/ggab054

Aubert J, Gastine T, Fournier A (2017) Spherical convective dynamos in the rapidly rotating asymptotic regime. J Fluid Mech 813:558–593

Aubert J, Livermore PW, Finlay CC, Fournier A, Gillet N (2022) A taxonomy of simulated geomagnetic jerks. Geophysical Journal International 231(1):650–672

Chulliat A, Maus S (2014) Geomagnetic secular acceleration, jerks, and a localized standing wave at the core surface from 2000 to 2010. J Geophys Res: Solid Earth 119(3):1531–1543

Finlay CC, Olsen N, Kotsiaros S, Gillet N, Tøffner-Clausen L (2016) Recent geomagnetic secular variation from Swarm. Earth, Planets and Space 68(1):1–18

Finlay CC, Kloss C, Olsen N, Hammer MD, Tøffner-Clausen L, Grayver A, Kuvshinov A (2020) The chaos-7 geomagnetic field model and observed changes in the south atlantic anomaly. Earth, Planets and Space 72(1):1–31

Gerick F, Jault D, Noir J (2021) Fast quasi-geostrophic magneto-coriolis modes in the earth's core. Geophys Res Lett p 2020GL090803

Gillet N, Jault D, Canet E, Fournier A (2010) Fast torsional waves and strong magnetic field within the Earth's core. Nature 465(7294):74

Gillet N, Gerick F, Jault D, Schwaiger T, Aubert J, Istas M (2022) Satellite magnetic data reveal interannual waves in earth,Äôs core. Proceedings of the National Academy of Sciences 119(13):e2115258,119

Hammer MD, Cox GA, Brown WJ, Beggan CD, Finlay CC (2021) Geomagnetic virtual observatories: monitoring geomagnetic secular variation with the swarm satellites. Earth, Planets and Space 73(1):1–22

Hide R (1966) Free hydromagnetic oscillations of the earth's core and the theory of the geomagnetic secular variation. Phil Trans R Soc London Series A, Mathematical and Physical Sciences 259(1107):615–647

Mandea M, Holme R, Pais A, Pinheiro K, Jackson A, Verbanac G (2010) Geomagnetic jerks: rapid core field variations and core dynamics. Space science reviews 155(1):147–175

Chapter 2

Descriptions of the datasets

2.1 Updated geomagnetic datasets, and data error covariance matrices (preliminary release at MS-2)

4DEarth_Swarm_Core ESA project deliverable CCN1 D-L.1

Chris Finlay, Magnus Hammer, Clemens Kloss and Nils Olsen
DTU Space, Technical University of Denmark

The report on geomagnetic datasets from the initial stage of the 4D Deep Earth Core project describes in detail the data products and models (Geomagnetic Virtual Observatories - GVOs, Ground Observatories - GOs, CHAOS geomagnetic field model) and their processing schemes – see Section § 2.1 (deliverable D-B.1) of the final version of the Scientific Report (before the start of CCN1). Below we document the updates and extensions of these datasets provided in this delivery.

2.1.1 updated GVO Datasets

A zip file containing updated Swarm GVO data files can be found at
`http://www.spacecenter.dk/files/magnetic-models/GVO/GVO_data_SWARM.zip`

This contains updated 4 monthly and 12 monthly GVOs produced using DTU's GVO software, and also (for completeness) the latest 1 monthly official Swarm GVO product (which involves additional processing steps applied by BGS). These were derived from Swarm L1B Mag-L OPER data version 0602. Data up to end of April 2023 was used for the 4 monthly and 1 monthly GVOs and data up to end of 2022 for the 12 monthly GVOs. No update of the Oersted, CHAMP, Cryosat-2 or Grace GVOs is provided in this delivery, the latest versions of these legacy missions are still those of the previous release – see associated zip folders for each mission at
`http://www.spacecenter.dk/files/magnetic-models/GVO/`

as there has been no change in the processing scheme.

Each GVO file includes values for observed field, core field (with estimates of magnetospheric and ionospheric fields removed) and SV (from annual difference of the core field data). The file format follows the Swarm Geomagnetic Virtual Observatories Product Definition, Rev.2B, SW-DS-DTU-GS-004_2-1_GVO_PDD. See Hammer et al (2021) for full details of the GVO processing algorithm. Further specific details regarding this update are found in the README file in the zipped folder.

2.1.2 Updated Ground Observatory data

A zip file containing updated GO data files in cdf format (following the ESA GVO file specifications) with 1monthly, 4monthly and annual averaging for data based

on hourly mean data from 1997 to 2023 at 218 Ground observatories (from the BGS AUX_OBS data product version 0136 from May 2023) can be found at:
http://www.spacecenter.dk/files/magnetic-models/GO/GO_data.zip

Each file contains the 'Observed' field (e.g. observed monthly means) and 'Core field' (e.g. revised monthly means) as well as SV derived as annual differences of the 'Core Field'. Full details of the processing of each data file and given in the file Readme_GO.txt inside the zip file.

This format has been successfully used within the consortium within the initial phase of the project e.g. by the Grenoble team. These are updated versions of the GO datasets described in the report of the initial phase of the Swarm+4D Deep Earth: Core project.

Refer to the archived_GO_files for earlier versions of the GO datafiles. These are labelled by version number.

2.1.3 Updated version of the CHAOS field model

Below are links to the CHAOS-7.15 geomagnetic field model, an updated version of the CHAOS-7 geomagnetic field model (Finlay et al, 2020), using Swarm baseline 0602 data up 8th June 2023 and ground observatory data up to end of May 2022 (based on the BGS AUX_OBS data product version 0136 from May 2023). Model coefficients for the time-dependent internal field are provided in spline coefficient and shc formats, while the .mat file contains all parts of the model. Links to software to read and use these files in Python, Matlab and Fortran can be found at:
http://www.spacecenter.dk/files/magnetic-models/CHAOS-7/index.html

2.1.4 Updated vector and scalar satellite data files as used in the CHAOS field model

The link below
http://www.spacecenter.dk/files/magnetic-models/CHAOS-7/CHAOS-7_15_data.zip
gives ascii files containing the selected vector and scalar satellite data (from the Swarm, CHAMP, Oersted and Cryosat-2 satellites) used in building the CHAOS-7.15 field model. These contain Swarm data up until early June 2023. The vector field is provided as components in an Earth centred, Earth fixed, spherical polar coordinate system (i.e. radial, southward, eastward components). Estimates of the crustal and external fields based on the CHAOS-7.15 model are also provide for each datum, so users interested in the core field can subtract these if wished. The file header specifies the exact content.

2.1.5 Full Covariance Matrix for Swarm 4 monthly GVOs

A full data error covariance matrix for the 4-monthly GVO SV product can be found at
`http://www.spacecenter.dk/files/magnetic-models/GVO/COV_GVO_4mon_SV_0101.txt`

Format is ascii, Covariance matrix of size 900x900 (900= 3 components at 300 GVOs) order as in GVO cdf files. If a covariance matrix for the core field is required, assuming uncorrelated errors in time one can use the above SV matrix (derived from annual differences of the core field) scaled by a factor 0.5. This was derived by the following procedure:

1. Load 4 monthly GVO product, core field or SV series
2. Remove large outliers w.r.t. CHAOS-7.15 field model
3. Compute a Gaussian Process fit to each component at each GVO location (squared exponential kernel).
4. Subtract this fit from observations.
5. Standardise the resulting residuals by removing the mean value and dividing by the standard deviation of the residuals from each component at each GVO.
6. Removed all time epochs with gaps in global coverage, except when only GVO was missing, in which case the missing value was replaced by zero.
7. Compute the non-linear Ledoit-Wolf estimator of the covariance matrix (Ledoit and Wolf, 2020) which results in a valid (symmetric, positive definite) covariance matrix.

The Ledoit-Wolf nonlinear shrinkage estimator is designed for estimating large covariance matrices. It is based on a minimum variance criteria and involves retaining all eigenvectors of the empirical covariance matrix but shrinking the eigenvalues based on a nonlinear analytic function of the eigenvalues, based on results from random matrix theory (Ledoit and Wolf, 2020).

Bibliography

Finlay CC, Kloss C, Olsen N, Hammer MD, Tøffner-Clausen L, Grayver A, Kuvshinov A (2020) The chaos-7 geomagnetic field model and observed changes in the south atlantic anomaly. Earth, Planets and Space 72(1):1–31

Hammer MD, Cox GA, Brown WJ, Beggan CD, Finlay CC (2021) Geomagnetic virtual observatories: monitoring geomagnetic secular variation with the swarm satellites. Earth, Planets and Space 73(1):1–22

Ledoit O, Wolf M (2020) Analytical nonlinear shrinkage of large-dimensional covariance matrices. The Annals of Statistics 48(5):3043–3065

2.2 Re-analyzed core motions over the satellite era

4DEarth_Swarm_Core ESA project deliverable CCN1 D-M.1

N. GILLET
ISTERRE

2.2.1 Initial proposition for Task M: a revised `pygeodyn` release and core flow models based on sparse estimators

The initial goal of task M was to provide an ensemble of re-analyzed core flow models inverted from satellite geomagnetic data, taking benefit of existing cross-covariances between two variables of the core state entering the `pygeodyn` assimilation software: the flow at large length-scales and the subgrid induction at large length-scales (Gillet et al, 2019). This source of information has so far been ignored when reconstructing flow models, and we thought that accounting for them would lead to reduce the uncertainty on the inferred core motions. Such cross-talking has been observed in simulations of the geodynamo (Gillet et al, 2022), in particular on the interannual time-scales of interest for wave-like motions. The correlation is particularly clear when considering the signature of the flow on the SV signal (see Figure 2.1). The relation between the various fields is summarized throught the induction equation once projected onto large length-scales, which in matrix form writes

$$\partial_t \mathbf{b} = \mathsf{A}(\mathbf{b})\mathbf{u} + \mathbf{e} = \mathbf{f} + \mathbf{e}\,, \tag{2.1}$$

where vectors $\mathbf{b}$, $\mathbf{u}$ and $\mathbf{e}$ store the parameters describing the magnetic field, the large scale flow and the subgrid induction terms. The vector $\mathbf{f}$ represents the induction from large-scale fields. The underlying rationale for a correlation between $\mathbf{u}$ and $\mathbf{e}$ is due to the fact that the flow on short length-scales (that enters the subgrid induction term) is correlated to the large-scale flow that is imaged (because the physics does not care about the spatial resolution of observations).

In the `pygeodyn` software, the forward model is based on a Wiener filter, which allows to estimate models from empirical samples in the sense of Least-Squares (LS). The forward model takes the form of a stochastic differential equation,

$$\partial_t \mathbf{z} = \mathsf{D}\mathbf{z} + \mathsf{B}\mathbf{w}\,, \tag{2.2}$$

where $\mathbf{z}^T = \left[\mathbf{u}^T\ \mathbf{e}^T\right]$ is the augmented model state, D is the drift matrix, B is a diffusion matrix and $\mathbf{w}$ a white noise. The model (2.2) is a multi-variate Auto-Regressive process of order 1 (or AR-1). For a model of size P, we seek for two matrices D and B, each of dimension $P \times P$. In this quest, the advantage of the LS formalism is its simplicity: the identification of the parameters is linear, and involves no ad hoc parameter. The drawback is its sensitivity to noise. This latter

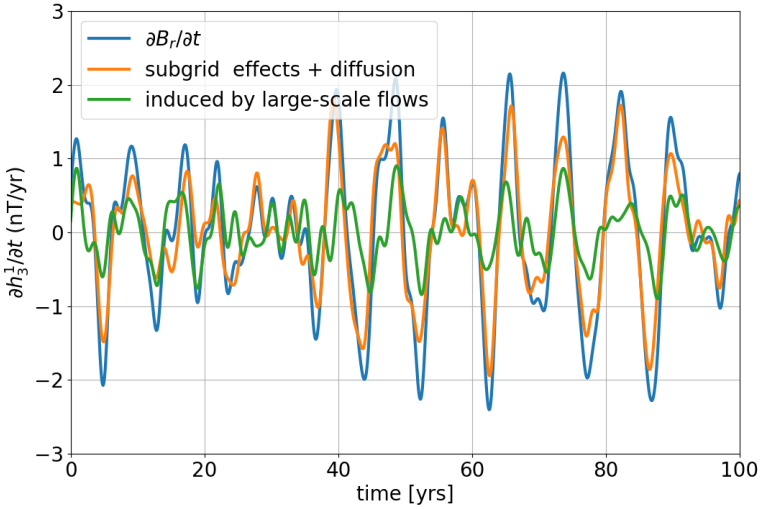

Figure 2.1: Secular variation for the gauss coefficient h_3^1 in the *71p* dynamo (blue), separated between an induction term associated with the large-scale flow (green), and the subgrid induction plus diffusion (orange). The series have been band-pass filtered at decadal periods. A clear correlation is observed between the two sources of magnetic field variations.

issue is particularly severe as the dimension of the model space increases, for a finite length of the sampled dynamo series.

In practice, `pygeodyn` is run with $P = P_u + P_e \simeq 400$, with $P_u = 200$ the dimension of the large-scale flow state $\mathbf{u}$ (once projected onto principal components), and $P_e = 195$ the dimension of the subgrid induction term $\mathbf{e}$ (truncated at spherical harmonic degree $L_e = 13$). This means $P^2 \approx 160,000$ entries for a model accounting for cross-covariances between $\mathbf{u}$ and $\mathbf{e}$ (resp. $40,000$ if considering instead two decorrelated fields, as operated so far). It is then tempting to search for algorithms allowing to build sparse models from empirical (dynamo) series. Together with P.-O. Amblard (statistician at the Gypsa-Lab, Grenoble) we derived and implemented the 'Alternative Direction Method of Multipliers' (ADMM, see Boyd et al, 2011) for deriving sparse drift and diffusion operators. We managed to produce sparse matrices as required. However, in practice this did not appear as a convincing strategy, because we realized that the correlation matrix between $\mathbf{u}$ and $\mathbf{e}$, that enter the construction of D and B, is by escence dense (which is not the case of correlation matrix between $\mathbf{f}$ and $\mathbf{e}$ where correlations are more easily detectable). If we partially recover the cross-talking between coefficients of vectors $\mathbf{e}$ and $\mathbf{f}$, the obtained correlations appear entached of noise, with a similar magnitude. We furthermore fail at unambiguously showing the benefit of the sparse algorithm, in comparison with the LS estimate.

We conclude at this stage that the novel approach initially envisionned for Task M, and the associated improvement of `pygeodyn`, comes to a dead-end.

2.2.2 New proposal for Task M: a revised `pygeodyn` release and core flow models based on higher order empirical models

Meanwhile, we realized that the noise within the ensemble of forecast trajectories was emphasized by one hypothesis behind the considered stochastic model (2.2): the limitation to a process of order 1. The motivation for such a model is associated with the temporal spectrum observed for $\partial_t \mathbf{b}$ (and thus $\mathbf{u}$), which behaves as $S(f) \propto f^{-2}$ for periods $1 \lesssim T = 1/f \lesssim 100\ yr$ (Lesur et al, 2018), while an process governed by an AR model of order p presents a PSD $\propto f^{-2p}$ towards high frequencies. However, the spectrum slope in simulations is steeper at frequencies higher than $O(1/T_A)$, where T_A is the Alfvén time (for the Earth one has $T_A = T_a^{\oplus} \approx 2$ yr). As a consequence, and AR-1 process will contain too much power on short time-scales, in comparison with a geophysical behavior. Recall that the plus of satellite geomagnetic data, as far as the core dynamics is concerned, is precisely towards short time-scales.

The choice of an AR-1 model was thus a good basis, but only in a restricted frequency range. In the *71p* simulation (Aubert and Gillet, 2021), one has $T_A^* \simeq 5.8$ yr, about three times the geophysical value. For this reason, the dynamo could not be sampled at a frequency shortest than $\approx 1/T_A^*$ when building an AR-1 model. In appears that some free runs of a *100p* dynamo are now available[1]. These simulations, run at closer to Earth-like parameters, present a $T_A^* \approx T_A^{\oplus}$. We have at hand 8 series, each covering about 100 yr.

In the above context, we thus propose to revise the deliverable for task M, taking benefit from the new simulations, by fitting higher order AR stochastic models. Spectra observed for the dynamo series (see Fig. 2.2) advocate for an AR-3 model, of the form

$$\partial_t^3 \mathbf{z} + \mathsf{A}_2 \partial_t^2 \mathbf{z} + \mathsf{A}_1 \partial_t \mathbf{z} + \mathsf{A}_0 \mathbf{z} = \mathsf{B}\mathbf{w}\,, \tag{2.3}$$

where matrices $\mathsf{A}_{0,1,2}$ and B are to be estimated from dynamo samples. To this purpose, we plan to use simultaneously

- the initial *71p* series (10 kyr long), sampled every $\Delta t^{71p} = 5$ yr,
- the new *100p* series, sampled every $\Delta t^{100p} = 0.2$ yr.

In practice a model such as (2.3) can be written with the same formalism as (2.2) for a modified state vector $\tilde{\mathbf{z}}^T = \left[\mathbf{z}^T\ \partial_t \mathbf{z}^T\ \partial_t^2 \mathbf{z}^T\right]$. Consequently, matrices $\mathsf{A}_{0,1,2}$ and B of the AR-3 model shall be derived using a LS formalism as performed today with an AR-1 model.

This will result in an improved version of the `pygeodyn` software, where:

[1] see https://4d-earth-swarm.univ-grenoble-alpes.fr/data

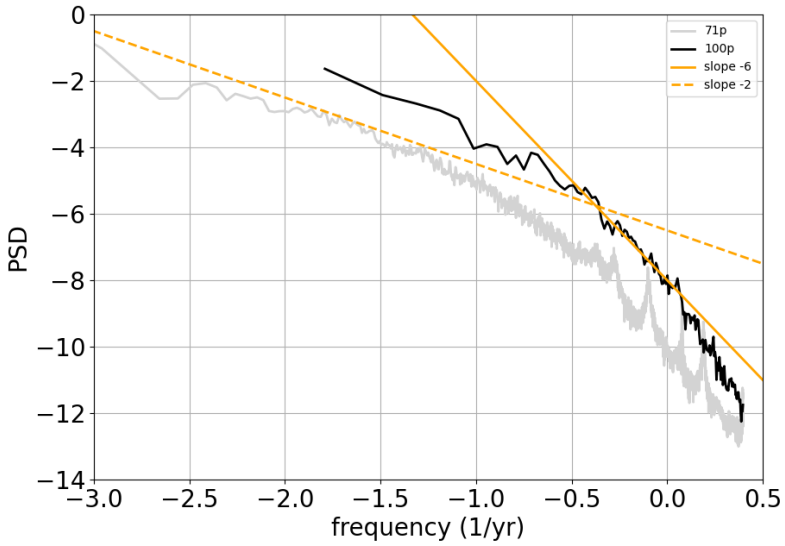

Figure 2.2: PSD for the core surface flow coefficient $t_2^{1,s}$, from the *71p* (grey) and *100* (black) dynamo series, superimposed with slopes $\propto f^{-2}$ (orange) and $\propto f^{-6}$ (dashed orange), characteristic respectively of an AR-1 and AR-3 models towards high frequencies.

- **The information provided from various simulations along the path (over various frequency ranges) can be simultaneously integrated, including the latest simulation presenting an Earth-like Alfvén time.**
- **The too high power present in the forecast at high frequencies shall be mitigated; this might be key since it exactly on short time-scales that satellite data are of greatest value for imaging the core dynamics.**
- **The resulting analysis will be directly smoothed according to the higher order equation considered. This shall help in isolating waves on short interannual periods in the inverted core surface flow models (Istas et al, 2023). It may also be crucial for imaging the electrical conductivity in the lower mantle, which is perceived as more conducting by core motions toward short time-scales (Firsov et al, submitted).**

Regarding the numerical implementation, the data assimilation tool (based on an ensemble Kalman filter, see Evensen, 2003) requires for each initialisation of the forecast (i.e., after each analysis where we adjust the model trajectory by incorporating observations) to know the model state at 3 successive forecast epochs. This shall be performed by simultaneously inverting magnetic data at three successive epochs, to obtain at each analysis step the model state plus its rate of change and curvature in time. As such, in the new `pygeodyn` release the revised algo-

rithm shall bring some of the benefits from the Kalman smoother (e.g. Cosme et al, 2010).

Revised deliverables for Task M

- Dataset D-M.1 at 01/09/19+54 months: ensemble of core flow models covering the period 1999-2024, obtained from the improved stochastic reanalysis tool, and updated geomagnetic satellite datasets (from Task L).
- Report R-M.1 at 01/09/19+54 months: a collaborative scientific study presenting the new developments on the pygeodyn software (implementation of the higher order model for the forecast and analysis steps), and illustrating the improvements they bring with respect to the original assimilation tool in terms of core flow reconstruction.

Deliverable D-M.1 was initially planned at KO+48 months. The new developments require to postpone by 6 months the production of the new flow models (thus at KO+54 months).

Revised risk assessment and failure scenarios for Task M

- The derivation of a higher order stochastic forward model simultaneously from the *71p* and *100p* dynamo data has already been performed. Its implementation into `pygeodyn` has been operated and tested by F. Dall'Asta, engineer at ISTerre.
- The subsequent modifications to the analysis step are currently being implemented into the software. In the case where the developments planned would not improve our recovery of transient motions, we would resort to the already working version of pygeodyn. This constitutes the failure scenario.
- The risk thus appears mitigated, as we already have at hand a `pydeodyn` tool that is operational. Even if the new tool was not developed in time, flow models over the considered period range could in any case be produced with the current version of the software.

Bibliography

Aubert J, Gillet N (2021) The interplay of fast waves and slow convection in geodynamo simulations nearing earth's core conditions. Geophys J Int DOI https://doi.org/10.1093/gji/ggab054

Boyd S, Parikh N, Chu E, Peleato B, Eckstein J, et al (2011) Distributed optimization and statistical learning via the alternating direction method of multipliers. Foundations and Trends® in Machine learning 3(1):1–122

Cosme E, Brankart JM, Verron J, Brasseur P, Krysta M (2010) Implementation of a reduced rank square-root smoother for high resolution ocean data assimilation. Ocean Modelling 33(1-2):87–100

Evensen G (2003) The ensemble kalman filter: Theoretical formulation and practical implementation. Ocean dynamics 53:343–367

Firsov I, Jault D, Gillet N, Aubert J, Mandea M (submitted) Radial shear in the flow at the earth,Äôs core surface. Geophys J Int

Gillet N, Huder L, Aubert J (2019) A reduced stochastic model of core surface dynamics based on geodynamo simulations. Geophys J Int 219(1):522–539

Gillet N, Gerick F, Jault D, Schwaiger T, Aubert J, Istas M (2022) Satellite magnetic data reveal interannual waves in earth,Äôs core. Proceedings of the National Academy of Sciences 119(13):e2115258,119

Istas M, Gillet N, Finlay C, Hammer M, Huder L (2023) Transient core surface dynamics from ground and satellite geomagnetic data. Geophys J Int 233(3):1890–1915

Lesur V, Wardinski I, Baerenzung J, Holschneider M (2018) On the frequency spectra of the core magnetic field gauss coefficients. Phys Earth Planet Int 276:145–158

2.3 An ensemble of 3D base states for Earth's core dynamics at epoch 2000 determined by geomagnetic data assimilation in a numerical geodynamo model

4DEarth_Swarm_Core ESA project deliverable CCN1 D-O.1

J. Aubert
IPG Paris

2.3.1 General description

This document refers to publicly available output data from a sequential framework that assimilates geomagnetic data into a numerical model of the geodynamo. The framework estimates the internal, three-dimensional state of Earth's inner and outer core according to the model, along a temporal trajectory punctuated by analysis points where the geomagnetic data at the core surface are combined with the internal dynamics of a background model, following an Kalman filtering strategy (see Aubert, 2015).

Mathematical models of the geomagnetic field (sets of spherical harmonic coefficients describing the core surface magnetic field and its rate-of-change, both up to spherical harmonic degree and order 13), are used as input data to the framework from epoch 1840 to epoch 2000. The geomagnetic field models COV-OBS (Gillet et al, 2013) is used to spin up the assimilation by performing 13 discrete analyses between epochs 1840 and 1990, after which a 14th analysis performed in epoch 2000 using the field model CHAOS-7-x9 (Finlay et al, 2020). While performing the analyses, the background geodynamo model is progressively advanced along a "path to Earth's core" in numerical simulation parameter space (Aubert et al, 2017), and reaches 43% along this path at epoch 2000.

The output data supplied here corresponds to the final base state at epoch 2000, that is suitable for subsequent theoretical and numerical work of the rapid dynamics that sets up on top of this base state throughout the satellite era 2000-2022. This state is not unique, because the variability of parts that are hidden to observation need to be estimated in a statistical way. What is supplied here is therefore an ensemble of 42 three-dimensional base states for the Earth's core at epoch 2000, that attempt to respect the statics (core surface magnetic field morphology) and kinematics (core surface magnetic field rate-of-change, associated core surface flow, leading order "QG-MAC" force balance) while adhering to the dynamical constraints enforced at this position along the parameter space path, and sampling the variability of hidden quantities.

2.3.2 Data format and description

The file format is MATLAB `.mat` in version 7.3 i.e. HDF5 compliant. The output uses a discretisation in physical space along the radial direction, while the lateral directions are described in a spectral way on a basis of spherical harmonics.

The file `Gauss_state.mat` contains:

- The radius vector `r(1:nr)` with `nr`=140, the number of radial grid points of the discretisation, and `ng=14`, the position of the inner-core boundary in the array `r(1:nr)`. The physical unit of `r` is km.
- The arrays `Bpnm(1:42,1:961,1:nr)` and `Btnm(1:42,1:961,1:nr)` respectively describing the 961 poloidal and toroidal spherical harmonic coefficients of the magnetic field, over the radial grid defined by `r(1:nr)` (hence comprising the electrically conducting inner core), and for the 42 members of the ensemble. The physical unit of `Bpnm` is T.km and that of `Btnm` is T.
- The arrays `Vpnm(1:42,1:961,1:nr-ng+1)` and `Vtnm(1:42,1:961,1:nr-ng+1)` respectively describing the 961 poloidal and toroidal spherical harmonic coefficients of the velocity field, over the radial grid defined by `r(ng:nr)` (hence excluding the inner core), and for the 42 members of the ensemble. The physical unit of `Vpnm` is $\mathrm{km}^2/\mathrm{yr}$ and that of `Vtnm` is km/yr.
- The array `Cnm(1:42,1:961,1:nr-ng+1)` describing the 961 poloidal and toroidal spherical harmonic coefficients of the density anomaly field, over the radial grid defined by `r(ng:nr)` (hence excluding the inner core), and for the 42 members of the ensemble. The physical unit of `Cnm` is kg/m^3.

Choosing a spherical coordinate frame with radius r, colatitude θ and the Greenwich-centered longitude φ, The poloidal-toroidal decomposition is adopted for the velocity field $\mathbf{u}$ and the magnetic field $\mathbf{B}$, such that:

$$\mathbf{u} = \nabla \times (Vt(r,\theta,\varphi)\mathbf{r}) + \nabla \times \nabla \times (Vp(r,\theta,\varphi)\mathbf{r}),$$
$$\mathbf{B} = \nabla \times (Bt(r,\theta,\varphi)\mathbf{r}) + \nabla \times \nabla \times (Bp(r,\theta,\varphi)\mathbf{r}).$$

Note that $\mathbf{r} = r\mathbf{e}_r$ is the **radius vector**, and **not** the radial unit vector $\mathbf{e}_r$. The density anomaly $C(r,\theta,\varphi)$ does not need such an expansion as it is a scalar field.

The scalar fields $X = Vt, Vp, Bt, Bp, C$ describing the velocity, magnetic vector fields as well as the scalar density anomaly field are supplied as real spherical harmonic coefficients $c_\ell^m(r)$ and $s_\ell^m(r)$ following

$$X(r,\theta,\varphi) = \sum_{\ell=0}^{30} \sum_{m=0}^{\ell} \left[c_\ell^m(r) \cos m\varphi + s_\ell^m(r) \sin m\varphi \right] P_\ell^m(\cos\theta)$$

Here P_ℓ^m is the Schmidt-seminormalised Legendre function of degree ℓ and order m. The base state is therefore supplied up to spherical harmonic degree and order

$\ell_{\max} = m_{\max} = 30$. For each ensemble member labelled i, and in the case where the inner core is included (i.e. the case of magnetic field coefficients), the ordering of radially discretized coefficients into MATLAB arrays follows:

$$\begin{aligned}
\texttt{Xnm}(i,1,[1:\texttt{nr}]) &= c_0^0(\texttt{r}[1:\texttt{nr}]) \\
\texttt{Xnm}(i,2,[1:\texttt{nr}]) &= c_1^0(\texttt{r}[1:\texttt{nr}]) \\
\texttt{Xnm}(i,3,[1:\texttt{nr}]) &= c_1^1(\texttt{r}[1:\texttt{nr}]) \\
\texttt{Xnm}(i,4,[1:\texttt{nr}]) &= s_1^1(\texttt{r}[1:\texttt{nr}]) \\
\texttt{Xnm}(i,5,[1:\texttt{nr}]) &= c_2^0(\texttt{r}[1:\texttt{nr}]) \\
\texttt{Xnm}(i,6,[1:\texttt{nr}]) &= c_2^1(\texttt{r}[1:\texttt{nr}]) \\
\texttt{Xnm}(i,7,[1:\texttt{nr}]) &= s_2^1(\texttt{r}[1:\texttt{nr}]) \\
\texttt{Xnm}(i,8,[1:\texttt{nr}]) &= c_2^2(\texttt{r}[1:\texttt{nr}]) \\
\texttt{Xnm}(i,9,[1:\texttt{nr}]) &= s_2^2(\texttt{r}[1:\texttt{nr}]) \\
&\ldots \\
\texttt{Xnm}(i,960,[1:\texttt{nr}]) &= c_{30}^{30}(\texttt{r}[1:\texttt{nr}]) \\
\texttt{Xnm}(i,961,[1:\texttt{nr}]) &= s_{30}^{30}(\texttt{r}[1:\texttt{nr}])
\end{aligned}$$

In the case where the inner core is excluded (velocity and density anomaly field coefficients) these relationships write e.g.:

$$\texttt{Xnm}(i,1,[1:\texttt{nr}-\texttt{ng}+1]) = c_0^0(\texttt{r}[\texttt{ng}:\texttt{nr}])$$

Note that the sinus coefficients corresponding to $m = 0$ are not stored as they vanish identically. Note also that unlike previous deliverables of this project, the coefficient c_0^0 is supplied because it is non-zero for the density anomaly field (but it is otherwise vanishing for all other solenoidal fields).

2.3.3 Graphics for validation

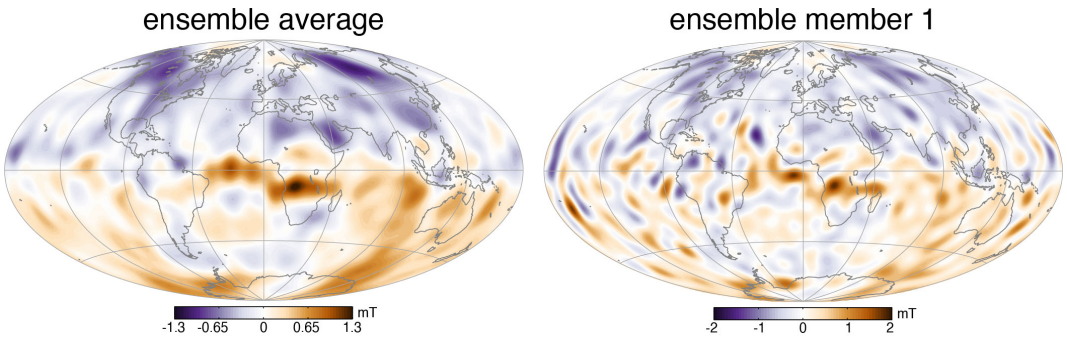

Figure 2.3: Hammer projection of the radial magnetic field at the external boundary (radial level `nr`=140) of the model, for the ensemble average (left) and first member of the ensemble (right).

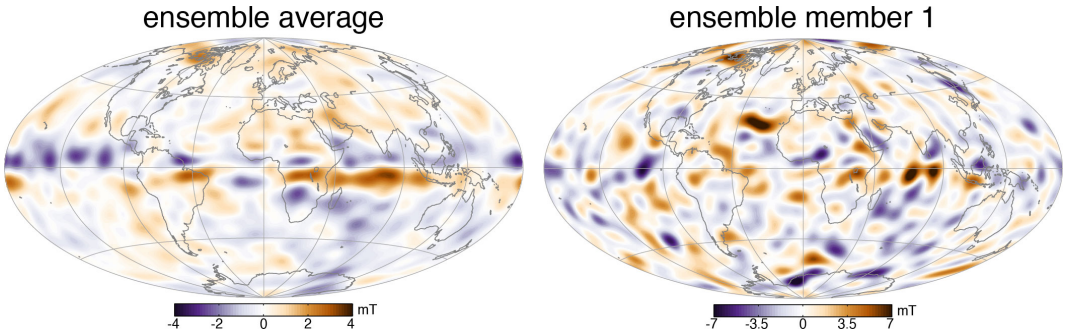

Figure 2.4: Hammer projection of the azimuthal magnetic field at the radial level `ir` = 121, corresponding to about 102 km below the core surface, for the ensemble average (left) and first member of the ensemble (right).

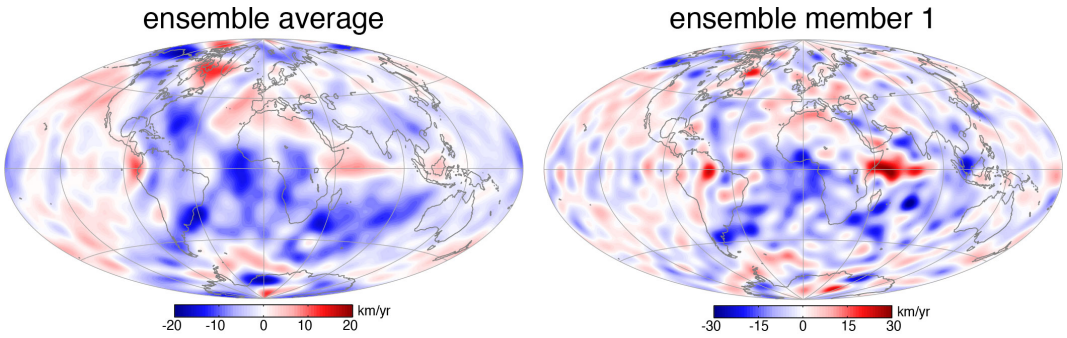

Figure 2.5: Hammer projection of the azimuthal velocity field at the external boundary (radial level `nr`=140) of the model, for the ensemble average (left) and first member of the ensemble (right).

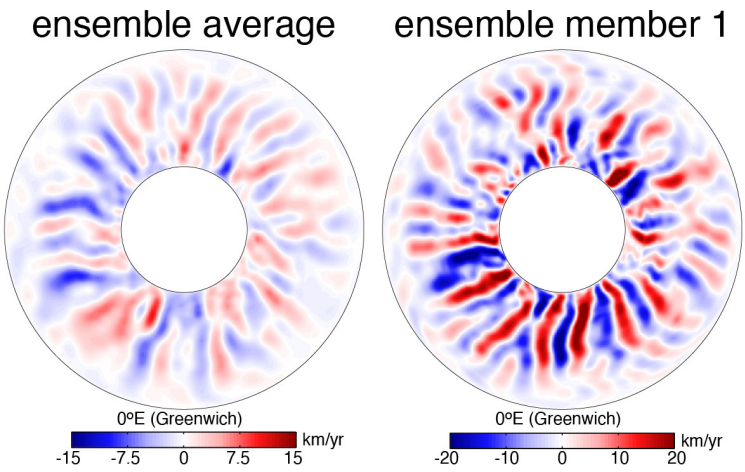

Figure 2.6: Radial velocity field in the equatorial plane, for the ensemble average (left) and first member of the ensemble (right).

Bibliography

Aubert J (2015) Geomagnetic forecasts driven by thermal wind dynamics in the Earth's core. Geophys J Int 203(3):1738–1751

Aubert J, Gastine T, Fournier A (2017) Spherical convective dynamos in the rapidly rotating asymptotic regime. J Fluid Mech 813:558–593

Finlay CC, Kloss C, Olsen N, Hammer MD, Tøffner-Clausen L, Grayver A, Kuvshinov A (2020) The chaos-7 geomagnetic field model and observed changes in the south atlantic anomaly. Earth, Planets and Space 72(1):1–31

Gillet N, Jault D, Finlay CC, Olsen N (2013) Stochastic modeling of the Earth's magnetic field: Inversion for covariances over the observatory era. Geochem Geophys Geosyst 14(4):766–786, DOI {10.1002/ggge.20041}

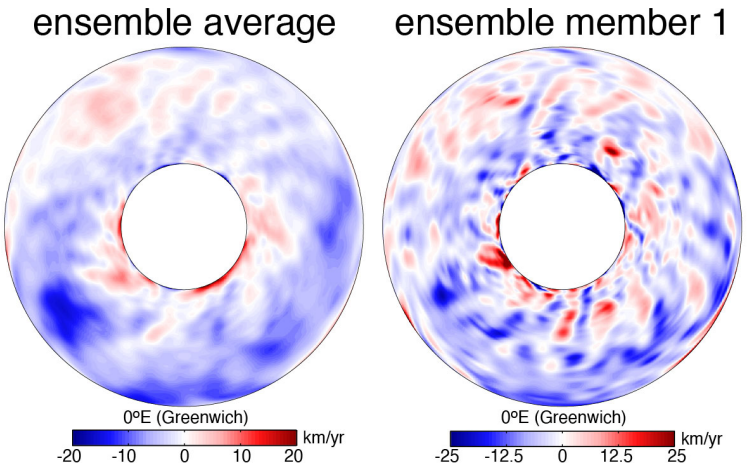

Figure 2.7: Azimuthal velocity field in the equatorial plane, for the ensemble average (left) and first member of the ensemble (right).

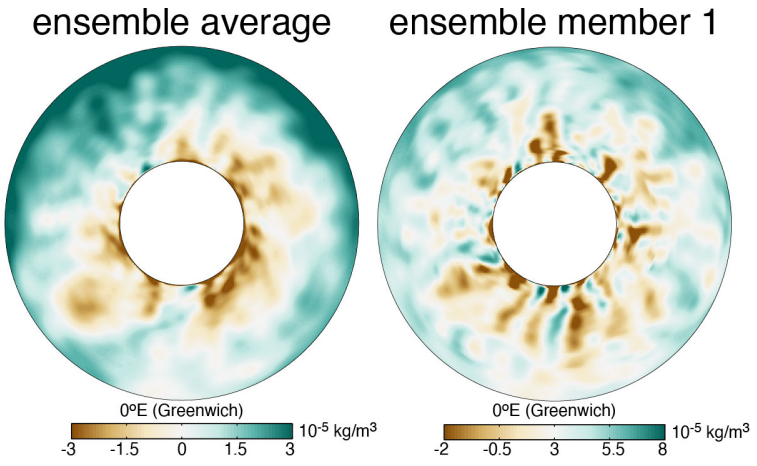

Figure 2.8: Density anomaly field in the equatorial plane, for the ensemble average (left) and first member of the ensemble (right).

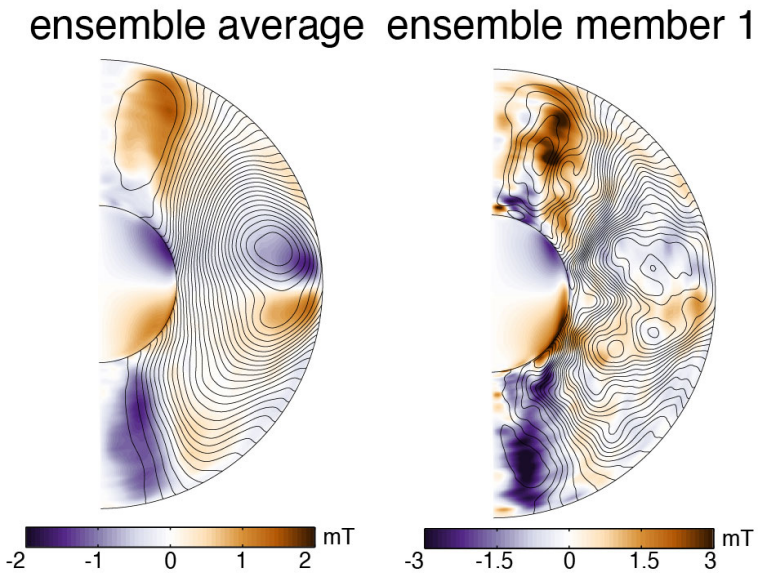

Figure 2.9: Meridional cut of the axisymmetrically-averaged azimuthal magnetic field, for the ensemble average (left) and first member of the ensemble (right). Overplotted are also the field lines corresponding to the azimuthally averaged poloidal magnetic field.

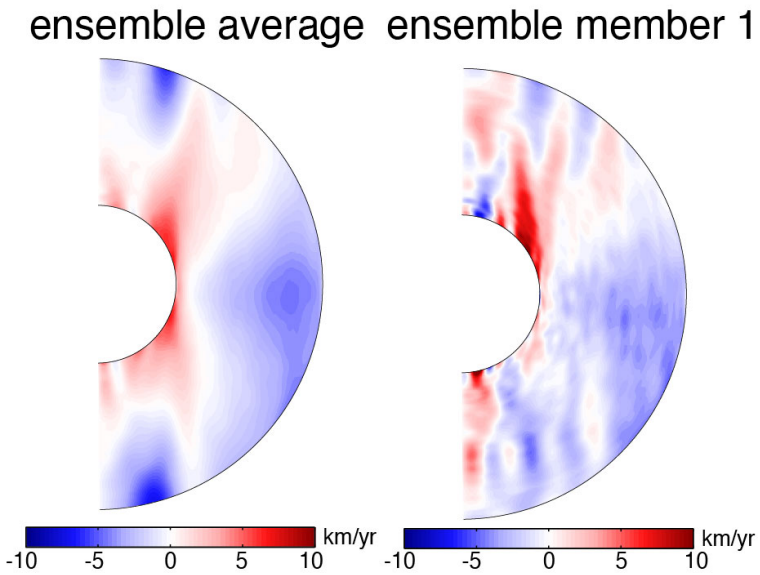

Figure 2.10: Meridional cut of the axisymmetrically-averaged azimuthal velocity field, for the ensemble average (left) and first member of the ensemble (right).

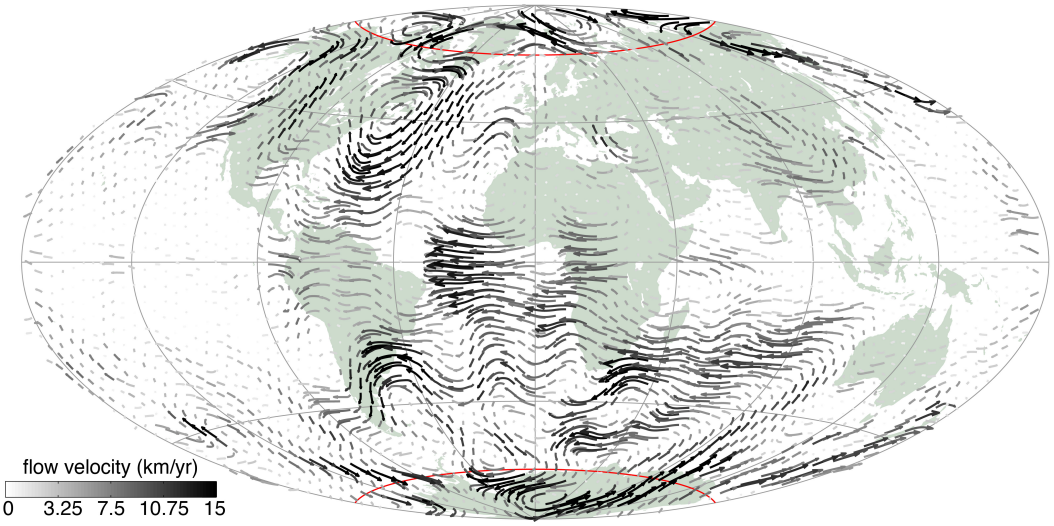

Figure 2.11: Quiver plot of the core surface velocity field for the ensemble average, in Hammer equatorial view, with the arrow greyscale representing the flow amplitude.

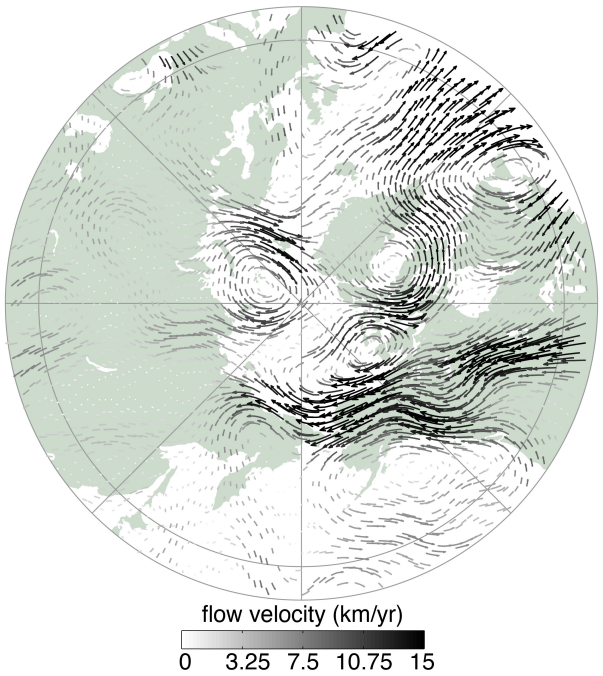

Figure 2.12: Quiver plot of the core surface velocity field for the ensemble average, in North polar view, with the arrow greyscale representing the flow amplitude.

Chapter 3

Insights on the deep Earth

3.1 Finding geomagnetic jerks in numerical models using a Bayesian transdimensional jerk-finding tool

4DEarth_Swarm_Core ESA project deliverable CCN1 R-N.1

P. Livermore
University of Leeds

3.1.1 Introduction

Geomagnetic jerks, abrupt changes in the local dynamics of magnetic field generation, were first identified as 'V'-shaped changes in the secular variation at ground-based observatories. Equivalent to step changes in the secular acceleration or an impulse in the third time derivative, these were quantified by either by fitting locally piecewise linear functions (e.g. Brown et al, 2013), or by wavelet analysis (Mandea et al, 2010). Using new numerical models, the existence of jerks has recently been tied to wave disturbances in the liquid core, both deep and shallow, that cause rapid changes in the magnetic field (Aubert and Finlay, 2019; Aubert et al, 2022). In principle the signature of jerks might be used to infer the background state of the core, which ultimately modulates any wave phenomena.

This report extends using a local analysis the recent study of Aubert and colleagues (Aubert et al, 2022), who investigated in some detail the causal mechanism of a variety of global jerk events from the 71% path geodynamo model (Aubert and Gillet, 2021). The model runs at 71% along a path, where 100% denotes Earth-like parameters. They produced a catalogue of jerks based on the spatially-averaged temporal jump in the second time derivative of the magnetic field (Aubert and Finlay, 2019), E_J, whose peaks signify a global jerk. The catalogue comprised 14 prominent events over the duration of the 10000 year, high-resolution dataset (between 4000 to 14000 years). These events were highlighted because they could be linked to clear dynamical changes within the core, although the model SV timeseries showed that many more weaker, or non-global, events occurred. If we can directly relate the recurrence time within the catalogue to Earth, we might expect that a prominent event would occur with a frequency about 14/10000 yr^{-1}, or one event every 700 years. This timescale is surprisingly long compared with the frequency that jerks appear in geomagnetic timeseries over the last few decades (Pavón-Carrasco et al, 2021): for instance, jerks in 2003, 2007, 2011, 2014, 2017, which suggests that the quasi-regular events that we observe for Earth are not the strongest possible.

Local analyses of jerks focus on finding 'V'-shapes in secular variation. One approach is to find the best-fit two-segment piecewise linear approximation to a timeseries (e.g. Pinheiro et al, 2011; Brown et al, 2013). While this is technically straightforward, the key limitation with is that the SV timeseries window needs

to be subjectively chosen. Usually, but not always, the timeseries is restricted to a window that includes a visually identified jerk event. Moreover, the timeseries must only include one jerk or the method will fail. Timeseries must be therefore be not too long, but neither can they be too short or noise (i.e. unmodelled signal) in observatory data will prevent reliable jerk detection. Unfortunately it not not yet possible to predict when jerks will occur, and it is not possible to objectively choose a suitable SV window length.

Here we explore the possibility of using a recently developed Bayesian method to find a piecewise linear fit to 10000-year-long SV timeseries from the 71% path geodynamo model (Aubert and Gillet, 2021). By construction, this will include all localised 'V' shaped signature of jerks. The method has two principal advantages over previous local analyses. First is that we do not need to subjectively cut the timeseries into short pieces, one per jerk, but rather treat the entire timeseries as a whole. Second is that we can quantify the uncertainty of jerk timing. This has been achieved in some probabilistic studies (Pinheiro et al, 2011; Brown et al, 2013) based on the likelihood (the probability of the data given a model). Here, we produce a measure of uncertainty based on the posterior probability, the probability of the jerk model given the SV dataset, which may be more appropriate.

3.1.2 A Bayesian jerk-finder tool

A probabilistic approach

There are two fundamental problems of fitting a piecewise linear function to a timeseries of SV. The first is that the timeseries contains signal other than piecewise linear (external signal in observatory data, but also unmodelled nonlinear signal). Therefore we seek a fit to within a reasonable tolerance but not an exact fit. Second is that we don't know how complex a piecewise linear function to fit (i.e. how many vertices). In this study, which is based on the method presented in Livermore et al (2018), we adopt a probabilistic approach producing a large ensemble of piecewise linear models that are (a) compatible with the given timeseries (within a defined tolerance), and (b) which have a number of linear segments which is not chosen by the user, but rather selected minimalistically by the data. This approach has the added benefit that the statistics of the ensemble has a clear and probabilistic interpretation whose marginal distributions can be used to identify jerks. For example, given the ensemble, we can calculate quantities such as the most likely time(s) at which there is a change in linear slope (i.e. when the jerks occurred), and their associated most likely change in slope (i.e. the amplitude of the jerk(s), what we will call Δ).

Our method is based on calculating the statistics of the posterior distribution of a piecewise linear model ($\mathbf{m}$) fit to a dataset $\mathbf{d}$

$$p(\mathbf{m}|\mathbf{d}) = Cp(\mathbf{m})\, p(\mathbf{d}|\mathbf{m}) \tag{3.1}$$

where C is a normalising constant. This equation describes Bayes' rule, in which

the probability of the model given the data (the posterior, left hand side) is proportional to the prior distribution (the first term on the right) multiplied by the likelihood (the second term on the right).

The model

Central to the method is the model $\mathbf{m}$, which describes a piecewise linear function defined over the time interval $[t_{start}, t_{end}]$ with k interior vertices (or change points). If the value of the function at t_{start} (t_{end}) is F_{start} (F_{end}), and each of the k internal vertices have coordinates (t_i, F_i), the function is described entirely by the vector

$$\mathbf{m} = \left(k, F_{start}, F_{end}, t_1, t_2, \ldots, t_k, F_1, F_2, \ldots, F_k\right).$$

The number of internal vertices $k \geqslant 0$ (and therefore the dimensionality of the problem) is unspecified (the problem is then termed transdimensional); marginal statistics of k are a diagnostic of the method.

Although there is no regularisation within our method, Bayesian models always favour low-dimensionality if the data allows (Sambridge et al, 2006). This is because although a higher k will in general permit a better data fit (i.e. higher likelihood), it also means that the prior is smaller in magnitude as the probability becomes spread over more dimensions (noting that, as a probability density, it needs to integrate to 1). Conversely, a low k means that the prior distribution is more concentrated so takes larger values, but the data fit likely will be worse. Thus there is a trade-off, with the highest values of the posterior (i.e. the most likely choice of k) occuring for the lowest values of k that are reasonably compatible with the data. For the problem of finding jerks, this means that model complexity, the number of interior vertices (or change points) is only increased if, and when, the data require. For the ensemble of models describing the posterior, the temporal distribution of changepoints then reflects the constraints of the data which are possibly on multiple timescales: faster dynamics require more changepoints, whereas slower dynamics require fewer.

Prior distributions

The posterior distribution depends upon our choices for the prior distribution, which describes what is known about the model before the introduction of the data. Our approach here is to formulate a prior which is as broad as possible (although noting that no prior is strictly uninformative (Jaynes, 2003)) with the expectation that the data will heavily constrain the posterior. We may write

$$p(\mathbf{m}) = p(\mathbf{m}|k)p(k)$$

and then further assume that, given k, all remaining components of $\mathbf{m}$ are independent:

$$p(\mathbf{m}|k) = p(F_{start})p(F_{end})\prod_{i=1}^{k} p(t_i)\prod_{i=1}^{k} p(F_i).$$

We assume that the time and value of each internal vertex is uniformly distributed:

$$p(t_i) = \begin{cases} (t_{end} - t_{start})^{-1} & t_{start} \leqslant t_i \leqslant t_{end} \\ 0 & \text{otherwise} \end{cases}$$

and

$$p(F_i) = \begin{cases} (F_{max} - F_{min})^{-1} & F_{min} \leqslant F_i \leqslant F_{max} \\ 0 & \text{otherwise} \end{cases} \tag{3.2}$$

for some given F_{min}, F_{max}. The end-point values are assumed to follow the same distribution as above.

Finally, we assume that k is uniformly distributed between 0 and k_{max} for some given k_{max}:

$$p(k) = \begin{cases} k_{max}^{-1} & 0 \leqslant k \leqslant k_{max} \\ 0 & \text{otherwise} \end{cases}$$

The likelihood

The remaining ingredient in the posterior is the likelihood function, which measures the probability of the data given a particular model $\mathbf{m}$. Taking each datum d_i (which has an associated time of $\tilde{t}_i$) in turn, we calculate the difference between d_i and the interpolating linear regression function $g(\tilde{t}_i)$. This mismatch is the model error, which we assume to be Gaussian distributed with mean 0 and standard deviation σ, and with each datum independent of the others. The likelihood is then given by

$$p(\mathbf{d}|\mathbf{m}) = Ae^{-\phi}, \qquad \phi = \sum_{i=1}^{N} \frac{\left(d_i - g(\tilde{t}_i)\right)^2}{2\sigma^2}$$

where A is a normalising constant.

The error budget σ, which will in general depend on time, must account for any unmodelled signal: that is, anything other than representing Earth's internal field with a piecewise linear function. We adopt a value $\sigma = 3nT/yr$ which allows us to recover jerks as reported in the literature (see discussion in §3.1.2).

We note that other techniques to estimate the uncertainty include using the misfit (Pinheiro et al, 2011) or co-estimating σ alongside the other model parameters (Bodin et al, 2012). Furthermore, our choice of a Gaussian likelihood is purely expedient, and it would be straightforward to adopt other distributions, for instance, with longer tails.

Numerical realisation

Although equation (3.1) gives a simple description for the posterior distribution in which all terms are known analytically, our goals for jerk finding require marginal distributions. For instance, in order to calculate the posterior distribution of change points with time, we need to marginalise (i.e. integrate out) all the other model

parameters (the F values, and k). Similarly, the posterior probability distribution of jerk amplitude with time requires marginalisation. Unfortunately, there is no direct way to calculate this from equation (1), and numerical methods are required. We use a reverse jump Monte Carlo Markov chain methodology to produce a large ensemble of models $\mathbf{m}$, whose statistics converge to the posterior distribution we seek to quantify. Models which are more probable occur with higher frequency, and marginalisation is straightforward by simply quantifying the frequency of specific features across the ensemble.

Reverse jump MCMC methods require the construction of a chain of models. Starting with the current model $\mathbf{m}$, a perturbed model $\tilde{\mathbf{m}}$ is proposed, which differs from the current model by a random change. If the proposed model passes an acceptance test based on its posterior probability it is adopted as the next model in the chain; if not, model $\mathbf{m}$ is duplicated and used as the next model. Proposed models which have a higher posterior probability than the current model are always accepted, whereas models which are less likely are only sometimes accepted, and in this way the chain describes a guided random walk through model space.

The perturbations that occur to the current model at every step are chosen randomly from three choices. Perturbations of type (1), which occur with probability $1/2$, select a vertex at random (say index i, which could be the end points or an internal vertex) and add a random value to F_i, distributed $N(0,\sigma^2_{change})$. Perturbations of type (2), which occur with probability $1/6$, select an internal vertex at random and move it in time by a random amount distributed $N(0,\sigma^2_{move})$. Perturbations of type (3a), which occur with probability $1/6$ insert a new internal vertex (i.e. vertex birth) at a uniformly distributed time t^* between t_{start} and t_{end}. The proposed vertex is assigned a value $g(t^*)+a$, where $g(t^*)$ is the value of the linearly interpolated regression under the current model at t^* and a is a random amount drawn from $N(0,\sigma^2_{birth})$. Finally, in perturbations of type (3b) which occurs with probability $1/6$, a random internal vertex is removed (i.e. vertex death).

The values $\sigma_{change}, \sigma_{move}, \sigma_{birth}$ control how efficiently the model space is sampled, and appropriate choices are key to ensure that the ensemble statistics converge rapidly. The values $\sigma_{change}, \sigma_{birth}$ are chosen to be the same as the likelihood error budget of 3 nT/yr; while the value σ_{move} is chosen as 1yr, approximately the minimum resolvable timescale of core dynamics from a single location (Backus et al, 1996).

From random parameter values for the initial model, we run the chain for a *burn-in* length of 10,000. We then collect the next 1,000,000 models in the chain, which is thinned to 10,000 (keeping every 100^{th} model). This procedure is adopted in order that the statistics are not biased by the choice of initial condition. In terms of the other parameters, we choose a value of K_{max} to be at least 100, and F_{min}, F_{max} to be the minimum and maximum values of the timeseries. Each calculation is checked to make sure that K_{max} is sufficiently large. With these sampling parameters, the probability that a given proposed model is accepted (under perturbations (1,2,3a,3b) as above) are approximately 40%, 30%, 2%, 2%, which provides effi-

cient sampling (Roberts, 1996).

Jerk diagnostics

To find geomagnetic jerks we use the ensemble in a two step process: finding times at which the probability of a changepoint is high, and then checking that the associated slope change is sufficiently large to qualify as a jerk, ruling out very shallow 'V' shapes. The method makes use of the marginal distribution of changepoint density with time (termed here as $C(t)$), and the 2D marginal distribution of slope change with change point time. These discrete distributions are efficiently calculated by binning the relevant quantities across the ensemble. The two steps then are:

1. Find the times t_i corresponding to distinct and prominent peaks in $C(t)$
2. For each peak t_i identified, test whether the modal slope change Δ_i exceeds a threshold.

In step (1), only prominent peaks are of interest to jerk identification, which we quantify using topographic prominence [1] and set the threshold to be the standard deviation of the distribution. We keep only peaks that are a minimum of one year apart. In step (2), restricting to a single event at time t_i produces a 1D probability density function of slope change at $t = t_i$. We define Δ_i to be the modal slope change for this event (its most likely value); if Δ_i exceeds a threshold which we take to be 1 nT/yr^2 in absolute value we classify the peak as a jerk.

For each peak at t_i we estimate error bounds on jerk timing by locally fitting a one-sided Gaussian curve to $C(t)$ on either side of the peak. Practically, we find the minimum $a > 0$, $b > 0$ such that $C(t_i - a) < \tau C(t_i)$ and $C(t_i + b) < \tau C(t_i)$. If $C(t)$ is Gaussian distributed, then $C(t)$ drops by a factor of $e^{-1/2} \approx 0.61$ at a time 1 standard deviation from its peak. Thus $\tau = 0.61$ gives approximately a 1-standard-deviation credible interval.

The thresholds for jerk-amplitude and prominence can be viewed as sensitivity parameters, and delineate rapid 'V'-shape changes in the SV from other events, which could be 'V' shapes with a very shallow gradient change, or smoother non-piecewise-linear changes. The values we have chosen here are able to characterise jerk events similar to other methods as reported in the literature (see subsection 3.1.2).

We note that there are other definitions of a jerk that can be made using the ensemble. For example, Aubert et al (2022) calculated the discrete posterior average absolute change in slope, which was then compared to a baseline value. However, measures based on the mean properties are less robust to extreme ensemble members than metrics based on the highest probability features, and are therefore slower to converge. For this reason, modal values are adopted in this report.

[1] implemented by the Python package Scipy

Synthetic examples

Here we illustrate the method by creating several secular variation timeseries which have an underlying exact piecewise linear dependence but with added noise. The aim here is to see how well our method can recover the known jerks.

Figure 3.1.2(a) shows a very simple, single 'V' shape over the time interval $[0, 100]$ yr with a change of slope of 4 nT/yr^2 at $t = 50$. The timeseries has been sampled yearly and Gaussian distributed noise (mean zero and standard deviation 3 nT/yr) has been added (fig 3.1.2(b)). This is now the dataset which we pass to the jerk-finder.

The resulting posterior distribution of the piecewise linear fits is shown in fig 3.1.2(b), in which the mean, median and modal models recover well the underlying 'V'-shape. Figure 3.1.2(c) shows that the marginal posterior distribution of the number of vertices peaks with a single vertex (consistent with the underlying behaviour) but that a higher number of vertices are possible with a much smaller probability. This is a good illustration of the parsimonious nature of Bayesian methods, which favours simple models when compatible with the data constraints.

In order to use the ensemble to find jerks, figure 3.1.2(d) shows that $C(t)$ has a single prominent peak at $t_1 = 50.2$ (using a temporal bin width of 0.1), from which we can compute the 1-standard deviation credible interval of $[50, 50.5]$, which noteably contains the correct value $t = 50$. Figure 3.1.2(e) shows the 2D histogram of slope change with timing, from which the most likely value of the change in slope is $\Delta_1 = -3.95$ nT/yr^2, thus qualifying the peak as a jerk. The recovered jerk timing and amplitude values are very close to $t = 50$, $\Delta = -4$. The final output of the jerk finder is summarised in figure 3.1.2(f) which shows the dataset alongside a vertical bar showing the amplitude of the single reported jerk whose width indicates the timing uncertainty.

In a second example shown in figure 3.2, we apply the method to a timeseries containing three jerks, associated with three increasingly severe changes in slope at $t = 20$, $t = 60$ and $t = 75$. We follow the same procedure as before: add noise, use the dataset as input for the jerk finder, and plot the same diagnostics as for the previous example. Figure 3.2(b) shows that again the ensemble finds the piecewise linear dependence, whose number of internal vertices peaks at 3 (figure 3.2(c)). Figure 3.2(d) shows three peaks in $C(t)$, whose value of Δ is sufficiently large to qualify as jerks (figures 3.2(e,f)). Each of the known changes in slope fall within the given uncertainty bounds for jerk timing. The uncertainty interval is broader for the weaker jerks than the most severe because the (assumed fixed) noise has a relatively large effect on the fit to the data; at these times the ensemble is correspondingly more diverse and the changepoint distribution more spread out.

Finding jerks in geomagnetic and simulated models

Having demonstrated that the methodology works well in simple synthetic cases, we now apply the method to a variety of global geomagnetic models in order to

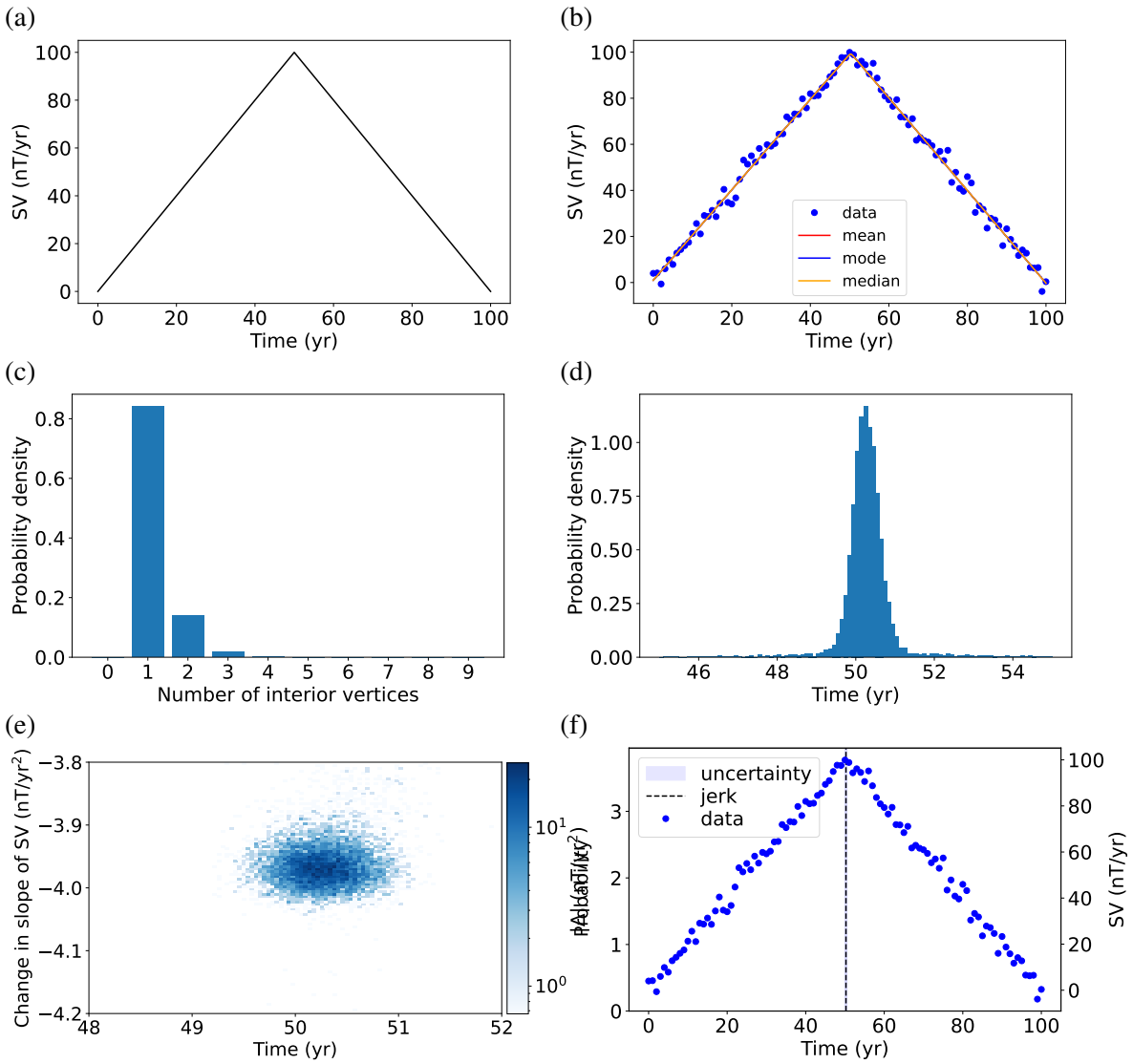

Figure 3.1: Finding jerks within a simple timeseries of secular variation. The original noise-free timeseries (a) is sampled yearly and 3 nT/yr noise is added (b). The mean, mode and median of the posterior distribution given this dataset is shown in (b), with the marginal distribution of the number of change points in (c) and their timing $C(t)$ in (d). Part (e) shows the 2D marginal discrete probability of the timing of the changepoints with their associated slope changes. Part (f) shows a summary: the data is shown as blue circles (right hand axis); the absolute amplitude of the jerk is shown as a dashed black line (left hand axis) with the timing uncertainty shown as light blue shading.

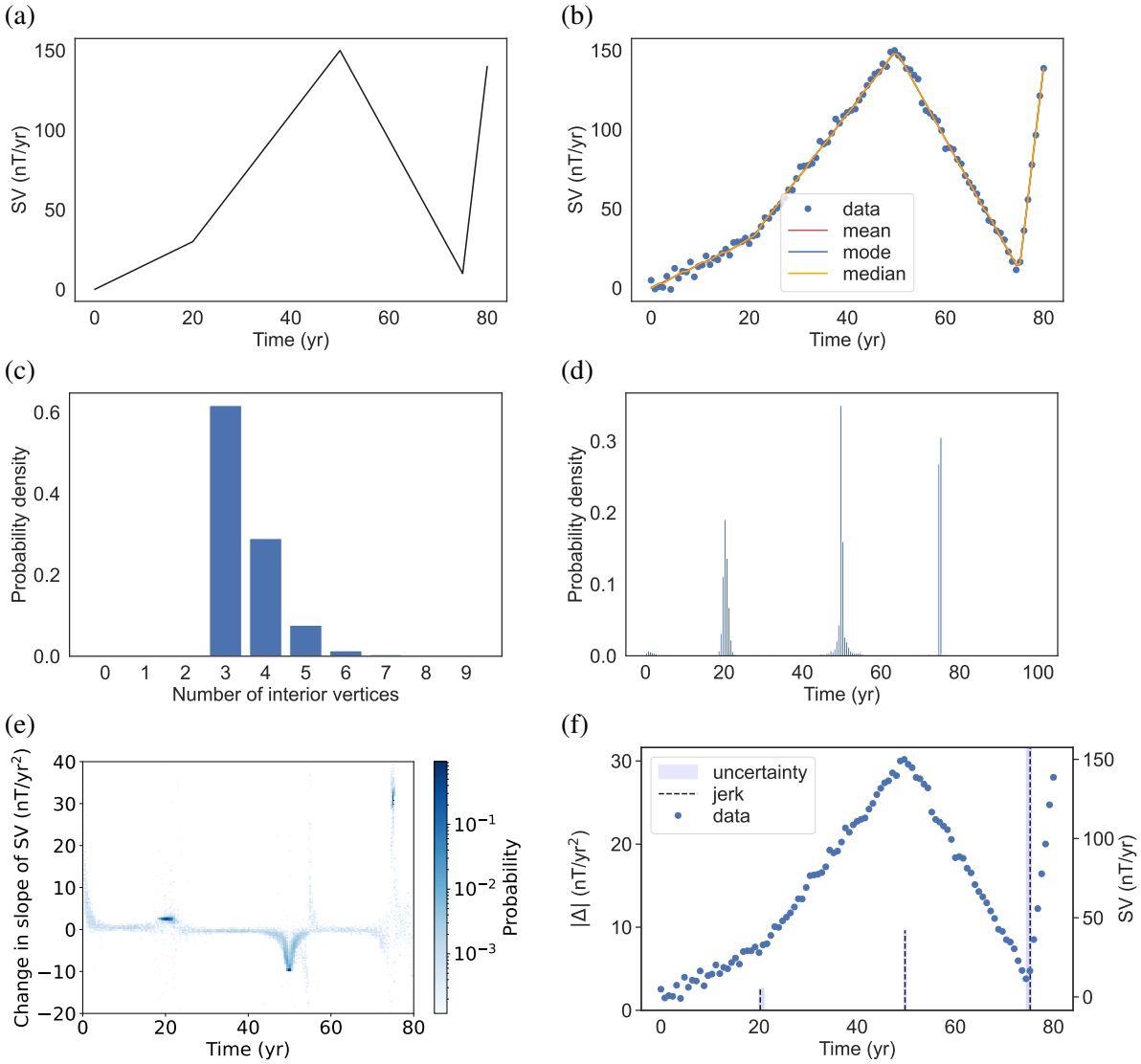

Figure 3.2: Finding jerks within a timeseries of secular variation containing three increasingly severe changes in slope at $t = 20, 50, 75$. An exact piecewise linear timeseries is sampled yearly (a) and 3 nT/yr noise is added. This data, with key diagnostics from the posterior distribution are shown in (b). The marginal distribution of the number of internal vertices is shown in (c) and their timing $C(t)$ in (d). Part (e) shows the 2D marginal discrete probability of the time of the changepoints with their associated slope changes. (f) shows a summary of the jerk finder: the data are shown as blue circles; the absolute amplitude of the jerk is shown as a dashed black line with the timing uncertainty shown as light blue shading.

confirm that our jerk classification agrees with results from previously published literature. We focus on global models, rather than observatory datasets, as ultimately our goal is to study the global 71% path model. However, we make comparisons with observatory data where possible.

Figure 3.3 shows the eastwood component of secular variation from three global geomagnetic models evaluated at the site of a geomagnetic observatory (a-c), with (d) showing a similar timeseries but from the 71% path model. We focus on the Y-component here as jerks are often more easily identified within this component in observatory datasets, but similar plots can be made using the other components with similar conclusions. Because of the discrepancy of jerk timescales of a factor of 3, we use yearly values of SV (from annual differences) for the 71% path model, whereas we use 4-monthly values of SV from the geomagnetic models.

Figure 3.3(a) shows the jerk around 1969/1970, one of the best known jerks in historical data, as seen at the Niemegk (Germany) observatory according to the CHAOS-1969 global model (Blangsbøll et al, 2022), plotted alongside observatory data. The jerk-finder identifies the jerk at 1970 with an amplitude of about 5 nT/yr^2, agreeing with previous studies (Blangsbøll et al, 2022). A weaker jerk is also seen around 1978 (Alexandrescu et al, 1995).

More recent secular variation from the era of continuous satellite monitoring using the CHAOS-7.14 model (Finlay et al, 2020) is shown in figure 3.3(b), where we have chosen to show the SV in Canberra (Australia). The analysis highlights the recent jerks (2011, 2014, 2017, 2020) in the Pacific region (Pavón-Carrasco et al, 2021); no jerks were found prior to 2012. Investigating a much longer timeseries, figure 3.3(c) shows secular variation from the mean COV-OBS.x2 model (Huder et al, 2020) over the period 1840 - 2020 in Honolulu (USA). The algorithm found 20 jerks, including widely documented events at 2004, 2011 and 2017, with the strongest jerk at 1930 with an amplitude of -7.5 nT/yr^2 (Alexandrescu et al, 1995).

Finally, we contrast these results with a timeseries drawn from the 71% path model in 3.3(d). We chose a 100 yr time window of secular variation containing the strongest global jerk event (at $t = 8880$) as documented by (Aubert et al, 2022). The jerk finder discovers jerks around $t = 8880$: interestingly not just one but 13 events, the largest magnitude of which has $\Delta = -40$nT/yr^2 and marks the first arrival of a train of oscillations. The jerks are much higher in amplitude than those from the geomagnetic SV timeseries, mainly due to the much increased scale range for the SV. Because the 71% path model has an Alfvén time that is three times longer than the Earth, the duration of any jerk event is too long by a factor of 3. Thus if this event were to be replicated in Earth, it would have a value of $\Delta \approx -120$nT/yr^2.

Choice of parameters

The purpose of the jerk-finding algorithm as described here is to discover jerks in a systematic manner which is as objective as possible: for example, avoiding the subjective windowing of the SV timeseries in order to fit one jerk at a time.

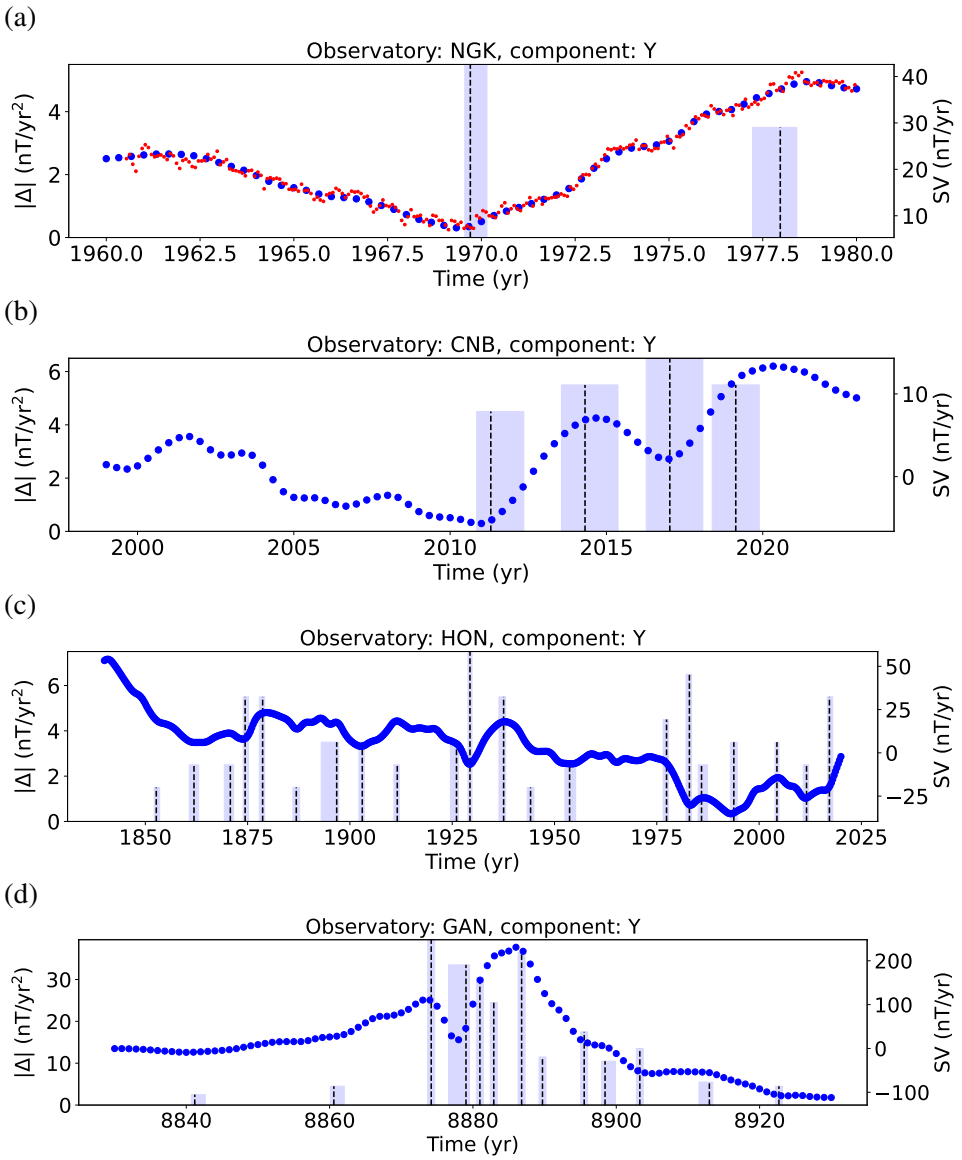

Figure 3.3: Application of the jerk-finder on geomagnetic and simulated datasets. (a) Y-component of secular variation at Niemegk according to the CHAOS-1969 global geomagnetic model from 1960-1980 (blue dots) with observatory data (small red dots); (b) Y-component of secular variation at Canberra observatory according to the CHAOS-7.14 model from 1999-2023 (blue dots); (c) Y-component of secular variation at Honolulu according to the COV-OBS.x2 model from 1840-2020 (blue dots); (d) Y-component of secular variation evaluated at Gan International Airport (Maldives) according to the 71% path model over the time interval [8830, 8930] (blue dots). In each case, jerks are shown by the vertical dashed lines, whose uncertainty is represented by the light blue vertical bar.

However, unavoidably there are parameters involved which need to be subjectively tuned.

One set of key parameters describe the prior density functions. However, we do not discuss these further as they are sufficiently broad to span most behaviour, and we assume that the constraints of the data predominate over any remaining dependence on the prior.

Possibly the most important of the remaining parameters is σ which describes the likelihood uncertainty. For secular variation timeseries derived from both global geomagnetic models and geomagnetic simulations, this uncertainty has two contributions. Firstly there is a time-dependent representation error, because the timeseries are not always exactly piecewise linear, and indeed the representation may be better at some times compared to others. Secondly there is model error due to the fact that neither dataset accurately describes the internal field. For the case of global geomagnetic models, this inaccuracy arises because of leakage from the external field due to incomplete separation of the internal and external fields; for numerical geodynamo models this arises from numerically misrepresenting the Earth, driven by inaccurate geodynamo non-dimensional parameters, energy sources or boundary conditions. From a practical viewpoint, σ is a measure of the data-fitting tolerance of the piecewise linear model which is is tantamount to a smoothing parameter. Large values of σ permit a large discrepancy to the data, but because of the inherent parsimonious nature of the method, badly-fitting low-dimensional models will be preferred over more complex but similarly badly fitting models (i.e. there will be oversmoothing). By contrast, smaller values of σ will require a close fit to the data and therefore (possibly) a complex model. It's worth pointing out that here "smoothing" means fitting using a smaller number of linear segments, not necessarily involving a piecewise linear representation with smaller gradients. We can therefore safely adopt the same value of σ for both geomagnetic and simulated models: because even though the timescales may differ for a jerk event, we would require the same number of linear segments to describe a jerk in each case (the changepoints in the geomagnetic case would simply be more compressed in time, compared to the simulation).

The value of $\sigma = 3$nT/yr we have chosen imposes an appropriate amount of smoothing that allows us to recover the same jerks as reported by other researchers. Ultimately this value is subjective however; taking a smaller value results in more jerks, and taking a larger value results in fewer jerks. Taking a uniform value across all models also allows direct comparison between analyses on different datasets. For example, the CHAOS-7 and COV-OBS.x2 models are both predominantly constrained by the same satellite data over 2000-2020, and our algorithm (with our choice of $\sigma = 3$nT/yr) finds the same jerks in each over this period. However, such agreement would not occur, for example, if σ was not constant but depended on diagnostics which differed between models. The disagreement would arise because σ (and therefore the smoothing) would be different in these two cases, and thus the jerk diagnostics would be different. One such diagnostic is the minimum to maximum range in SV over the whole model (as adopted in (Aubert et al, 2022)).

3.1.3 Jerks within the 71% path model

Having demonstrated that the Bayesian algorithm works on sample datasets, we are now in a position to apply the jerk-finder to timeseries from the entire 71% path model evaluated on a grid of points on the Earth's surface.

Long timeseries

Long timeseries are challenging to handle with the MCMC algorithm as the modal number of linear segments is likely very large. Based on the examples in subsection 3.1.2, we approximately require about 1 linear segment per 5 years. A single complete timeseries from the 71% path model (sampled yearly, from 4200 to 14,200), would then require about 2000 linear segments. This should be contrasted with the 100-year long examples in figure 3.3 which require only about 20 segments. Because the Markov chain length required to explore N degrees of freedom scales exponentially with N, even a modest increase in N can amount to a massive increase in computational time. For long time series, this computational cost is compounded by the increase of each individual proposed model comparison simply due to there being more data in the likelihood calculation.

Our approach instead is to divide a long time interval into sequential shorter windows of length 400 years. We can apply the MCMC algorithm on each window separately, and simply concatenate the resulting histograms of jerk statistics. We note that this is quite different to dividing the SV timeseries into single-jerk time windows; here, each 400 year timeseries contains numerous jerks. To ensure that there are no edge effects in the construction of the ensemble, we include an overlap of 50 years on each side (except at the end points) for the MCMC algorithm, which is then ignored when collecting the statistics. Thus we separate the range 4200 to 14,200 into 25 time windows [4200,4650], [4550,5050], and so on. Applying the MCMC algorithm to each window individually produces converged results with a chain length of only 1M. By performing 25 separate calculations, one for each time window, we can then analyse the whole timeseries at modest computational expense.

Figure 3.4 shows how the 10,000 years of the path model is divided into 400 year windows (the overlaps at either end of each window are not shown), illustrated by a timeseries of the Y-component of SV on the geographic equator at 45° longitude, the approximate location of one of the strongest events from the jerk catalogue at $t = 8880$ yrs. The results of applying the MCMC algorithm to one of these windows [8600,9000] is shown in figure 3.5. In all components, there are clusters of jerks both around $t = 8880$ and $t = 8700$ with the strongest in the Z-component around $t = 8880$ with a value of $|\Delta|$ of 36 nT/yr^2. The MCMC method therefore finds evidence of strong jerk events at $t = 8880$, a timing that agrees with the jerk energy global analysis of Aubert et al (2022) (see bottom panel of figure 3.5), defined as

$$E_J = < ([\partial_t^2 \mathbf{B}]_t^{t+3} - [\partial_t^2 \mathbf{B}]_{t-3}^{t})^2 > \tag{3.3}$$

where $< >$ denotes a global average and $[\ ]$ denotes a time average Interestingly the jerks identified around $t = 8700$ do not feature in the global diagnostic and so must therefore be local, rather than global events.

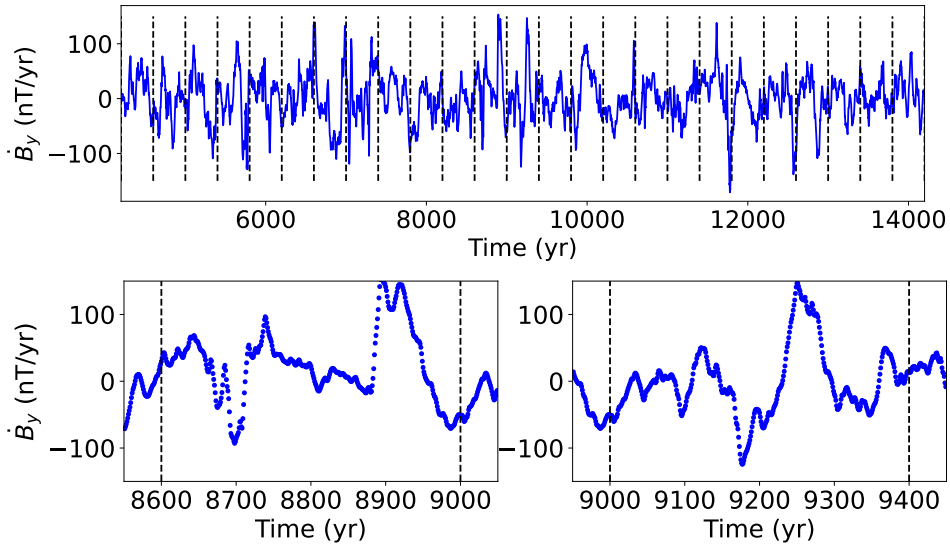

Figure 3.4: The top row shows the decomposition of the 10,000 years of the 71% path model into 400 year windows, illustrated by yearly values of the Y component of SV at colatitude 90° and longitude 45°. The bottom row shows two illustrative 400-year windows with 50 years of overlap at either side.

Jerk occurence

The results from an entire timeseries of SV at a single location (colatitude 90° and longitude 45°) are shown in figure 3.6, alongside a comparison to the global jerk energy. It is difficult to see the details as the timescale is too compressed, and it is clear that simpler diagnostics are required to probe the results. Nevertheless, we can identify that the major jerks in the different field components occur at similar times, although the magnitude of the jerks differs between the components, with the strongest in the Z component. Each of the peaks in E_J has a corresponding peak in the MCMC analysis of one of the components: that is, the global jerks have a local expression. The converse is mostly but not always true: strong local jerks ($\Delta \approx 25\text{nT/yr}^2$) occur in B_Z around $t = 11,500$yrs without any notable signature in E_J. The fact that jerks are often strongest in the Z component has been previously reported by several works (Olsen and Mandea, 2007; Aubert et al, 2022; Hellio et al, 2014), and may be related to the fact that (due to the geometry) B_Z has a higher magnitude than the other components.

Figure 3.7(left) shows a 100yr segment of the complete timeseries, centred $t =$ 8880, one of the strongest global jerks, driven by a shallow-wave. It is noteworthy

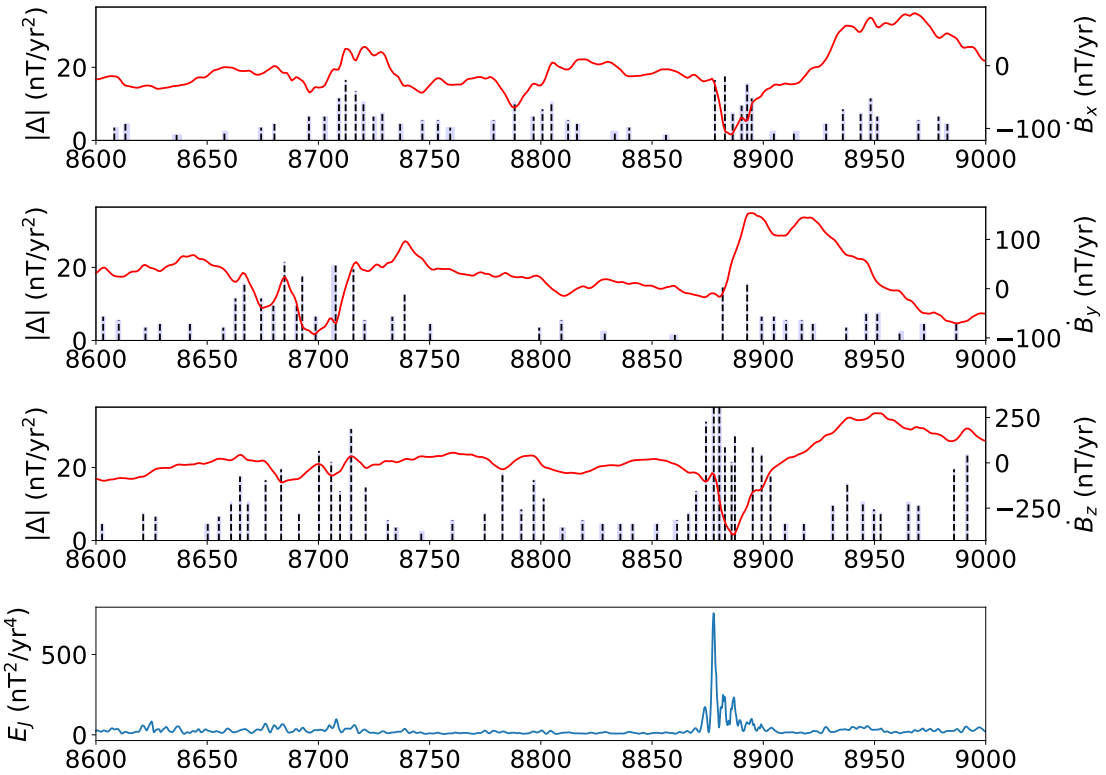

Figure 3.5: An example 400 year window from the 71% path model of the SV at Earth's surface at colatitude 90° and longitude 45°. Red shows the three components of SV (right axis), while the jerks are shown by the vertical dashed lines with uncertainty shaded in light blue. The bottom row shows the global diagnostic jerk energy of Aubert et al (2022) for comparison.

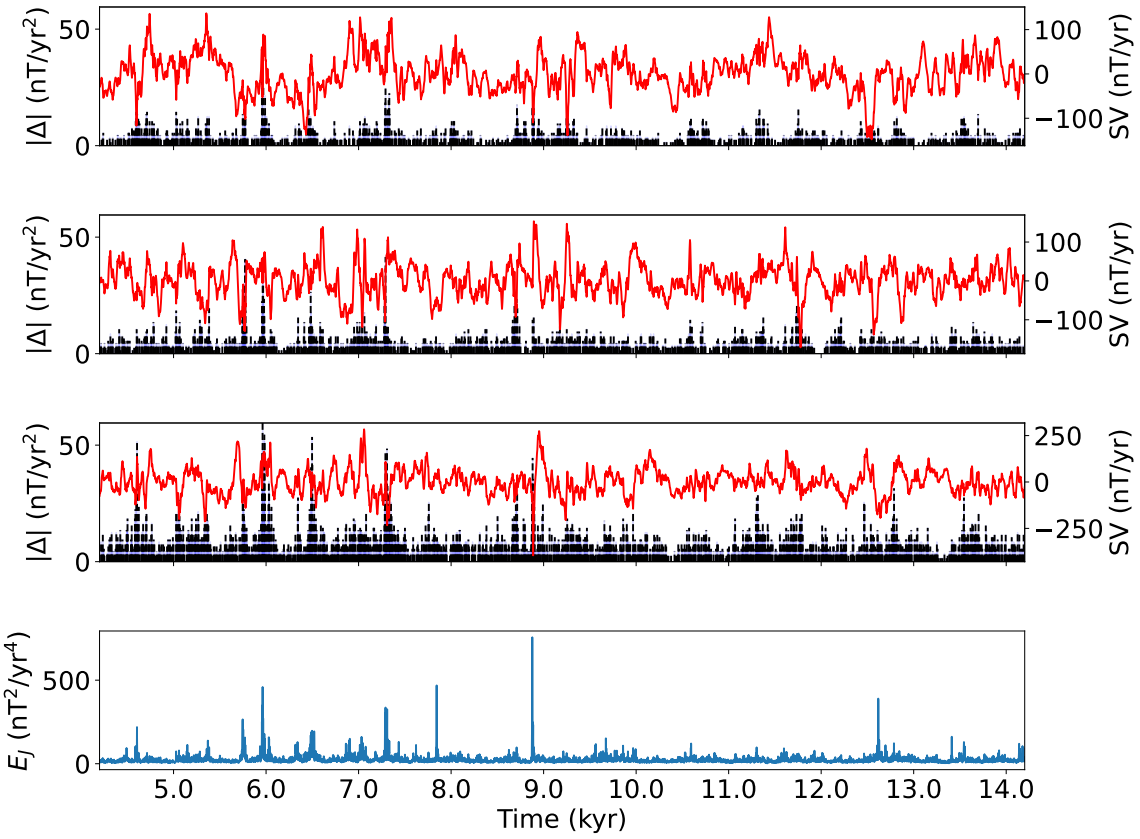

Figure 3.6: Jerk analysis of an entire timeseries from the 71% path model at colatitude 90° and longitude 45°. The top three panels show the X, Y and Z components of SV (red), with the jerks as dashed lines. The bottom panel shows the global jerk energy diagnostic for comparison.

that although jerks occur in all three components approximately at the same time, the number of jerks around the $t = 8880$ event, their amplitude and their exact timing are not the same. Indeed, jerks occur earliest in the Z component and have a stronger signature; there is a delay of about 1-2 years between the first major jerk in the Z component around $t = 8880$ and its counterpart in the X and Z components. This temporal offset is in agreement with geomagnetic observations and arises because of the different spatial sensitivity of the components on Earth's surface to the magnetic source on the core-mantle boundary. Overall, the event lasts about 20 years (between $t = 8880$ and $t = 8900$. We contrast this to a weaker event around $t = 13543$ (driven by a deep wave). The signature is still dominated by the Z-component, but interestingly the event seems more protracted and seems to extend to (at least) the entire 100 year time window shown.

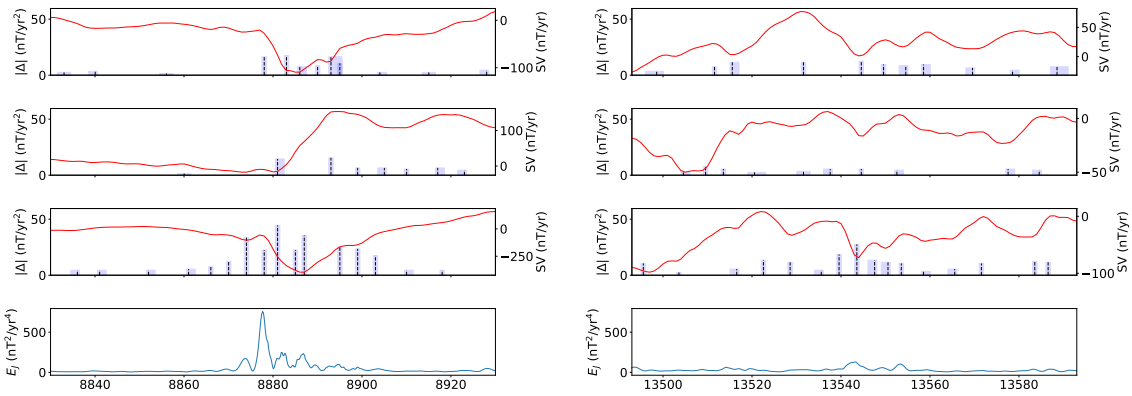

Figure 3.7: Jerk analysis of an entire timeseries but shown only for the 100yr period centred at $t = 8880$, one of the strongest global jerks (SW), at colatitude 90° and longitude 45° (left) and at $t = 13543$ (right), a DW event The top three panels show the X, Y and Z components of SV (red), with the jerks as dashed lines. The bottom panel shows the global jerk energy diagnostic for comparison. Although the jerk signature broadly aligns in all three components, in detail, neither the number of jerks, their strength or their timing agree between the three magnetic components. The SW event is very short, whereas the DW event is more protracted.

One way of characterising global jerk activity is to take the time-dependent maximum value of jerk activity over Earth's surface. We calculate this by quantifying the maximum value of $|\Delta|$ over all of the spatial locations on the 5x5 degree grid in yearly time bins. Figure 3.8 shows the results of this for each of the components (upper three panels) along with the maximum over all components (bottom panel). The peaks in the global jerk energy all align with peaks in the maximum value of E_J, showing that the local and global analyses agree well. However, the local method finds many more strong local jerks than appear in E_J: there are 233

years in which $|\Delta_Z|^{max}$ exceeds 40nT/yr^2. Thus we find at least 233 locally dominant events, in contrast to 14 globally dominant events in E_J.

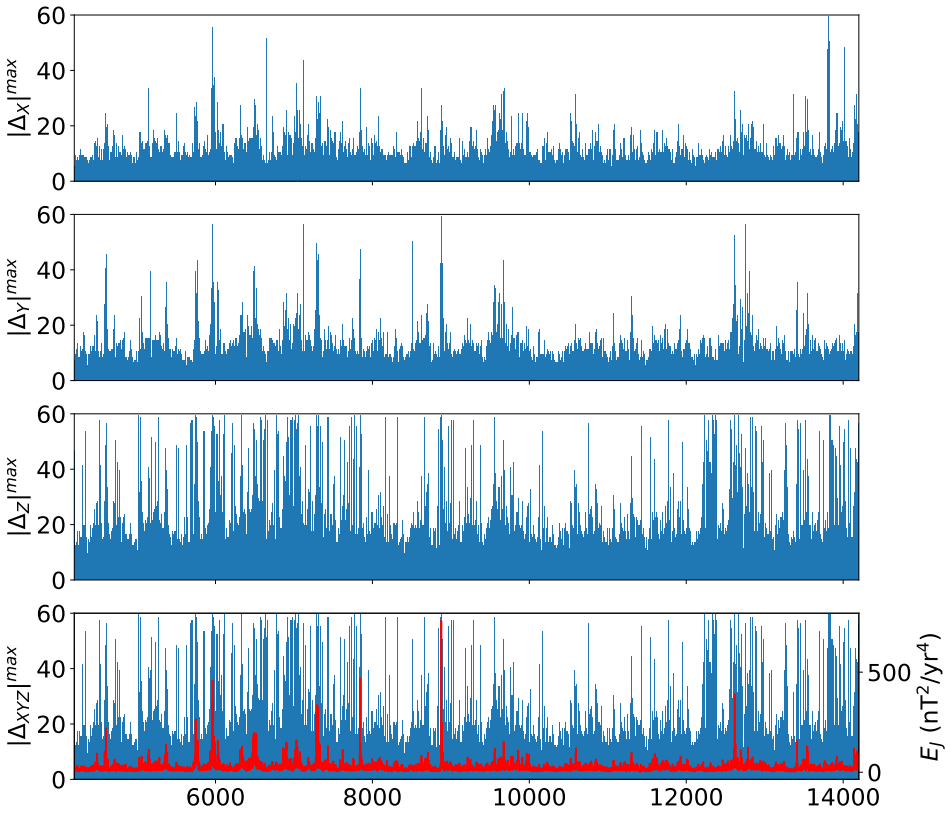

Figure 3.8: Maximum $|\Delta|$ over all spatial locations as a function of time, for each component (upper three panels). The lower panel is the maximum value over all components, overlaid by the global jerk energy diagnostic. All the $|\Delta|$ diagnostics shown have units of nT/yr^2.

It is also of interest to probe how often a jerk event occurs in the 71% path model. Figure 3.8 shows that in all years there is some jerk activity, that is ($|\Delta| > 1$) somewhere on Earth's surface. Thus at no time is the modelled Earth "quiet" with no jerk activity: jerks are a ubiquitous feature.

Another diagnostic of interest is to quantify how often jerks of different strengths occur. Counting the number of years that the spatial maximum of $|\Delta|$ exceeds a threshold allows us to calculate the recurrence time of a jerk event that may occur anywhere on Earth's surface. Figure 3.9 shows that larger events occur most frequently in the Z component, followed by the Y and X components respectively. For example, jerks that exceed 40nT/yr^2 occur every 1400, 300, 30 years for the X, Y and Z components. Another point of interest is that for weaker events (up to about 5nT/yr^2), jerks occur with the same yearly frequency in all three components. Thus weak events occur every year in all components, but stronger events

occur less frequency and predominantly in the Z component.

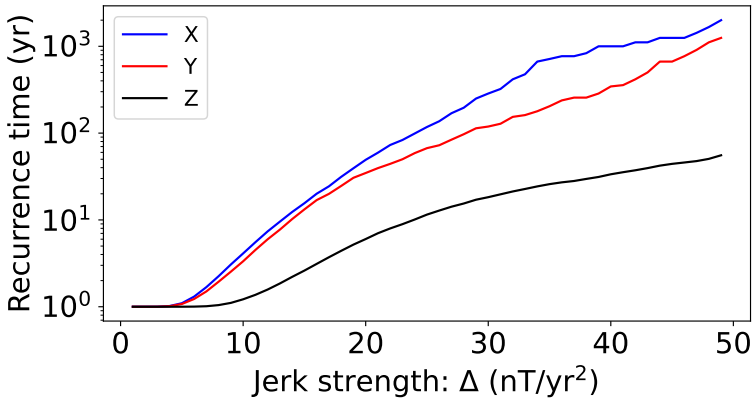

Figure 3.9: Recurrence time of jerk events with $|\Delta|^{max}$ exceeding a given threshold anywhere on Earth's surface, for each component.

On a global scale jerks have been shown to be ubitquitous, but locally this may not be the case. At any location on the Earth's surface, we can compute a pdf of the inter-jerk time interval. Figure 3.10 shows globally-averaged pdfs for the inter-jerk interval for the three magnetic components separately, and taken together. Compared with the X and Y components, the Z-component has a distribution which favours a shorter inter-jerk time, thus on average has frequent events. The modal wait time between jerks is about 5 yrs (with a mean value of about 10 yrs) in both any component or stacking the components, but the long tail indicates that some locations have a much longer wait in between events. Over the 10000 years, the maximum inter-jerk wait time occuring between events is 260 years, which occurs in the Y-component of SV at colatitude 120° and longitude -150.0°. Figure 3.11 shows histograms of the jerk amplitude stacked over all spatial locations. The histograms for the X and Y components have a similar shape (both with mean 4nT/yr^2, but that of the Z component (with mean 6nT/yr^2) has a longer tail towards the right which skews the distribution. Thus, of those events classified as jerks, the Z-component has a higher proportion of high amplitude jerks. Overall, not only are jerks more frequent in the Z-component they are stronger too: thus explaining the relatively low recurrence time for high amplitude events.

Spatial distribution of jerks

We now turn to the spatial distribution of geomagnetic jerks in the 71% path model. Figure 3.12 shows the maximum absolute jerk amplitude as a function of spatial location over the entire 10000 timeseries.

The strongest jerk activity occurs in the 90° longitude sector centred around the Indian ocean. The largest amplitude jerks occur in the Z-component, while the X and Y component see weaker events. This spatial preference is related to

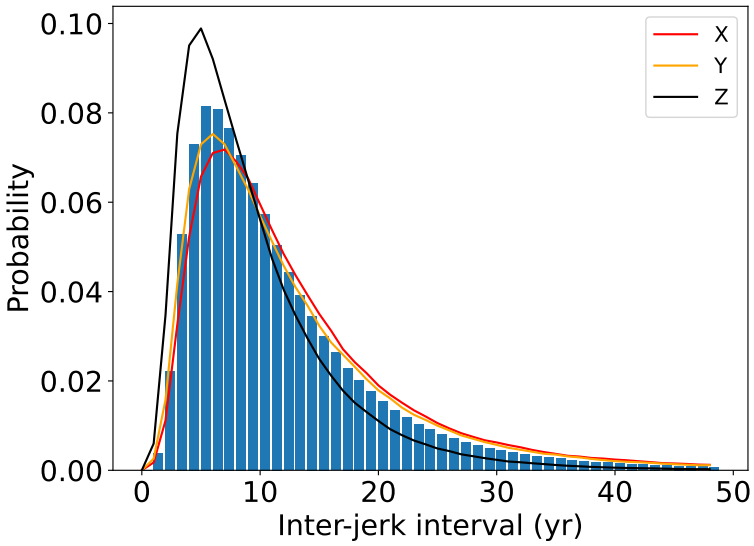

Figure 3.10: Global average of the spatially localised inter-jerk time interval, over all components. The modal wait time for the globally-averaged pdf for a jerk in any component is 5yrs.

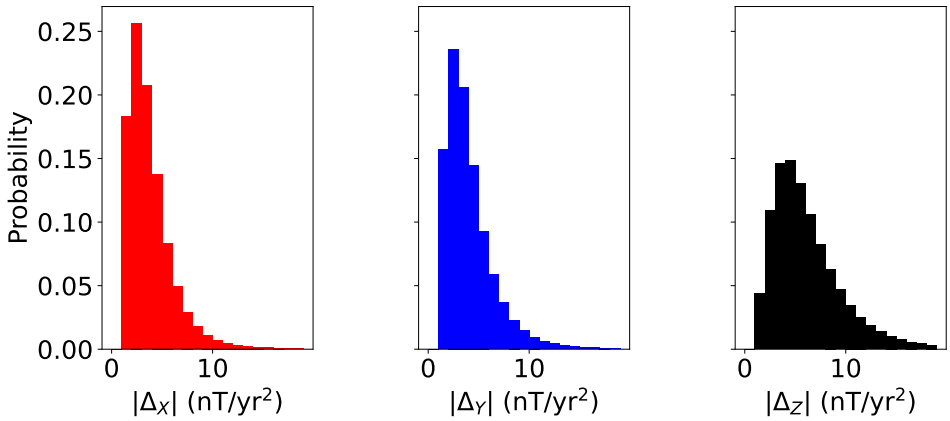

Figure 3.11: Histogram of jerk amplitude for each component, stacked over all spatial locations.

the inner-core boundary condition of the path model, at which there is a maximum mass anomaly release beneath Indonesia (see Aubert et al, 2013).

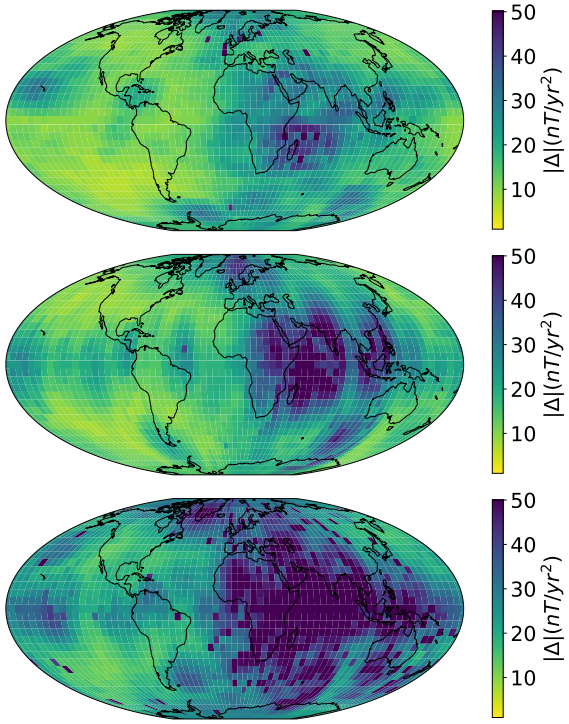

Figure 3.12: Plots of the temporally maximum value of $|\Delta|$ over the 10000 year timeseries from the 71% path model, for the three magnetic components X (top), Y (middle), Z (bottom).

We noted earlier that the jerks appear to separate into either weak events ($|\Delta| < 5$) which occur somewhere on Earth's surface every year, and stronger events with $|\Delta| > 5$ which have a longer recurrence time.

Figure 3.13 shows the average frequency of various strengths of jerk (weak, strong, extreme) attained by simply counting the number of events in each category over the 10000 years of the 71% model. In the top row, we see that weak events occur with a spatially uniform frequency of about 5 events per 100 years, consistent with the previously documented result that a weak jerk occurs *somewhere* every year. Stronger jerks occur with comparable frequency (10 per 100 years) but they are focussed over the Indian ocean. Extreme jerks only occur with a frequency of 5 per 100 years and are again focussed over the Indian ocean.

We see therefore two distinct behaviours: weak jerks that occur about every 20 years everywhere, without any spatial preference; and strong jerks that occur (in this model) preferentially around the Indian ocean.

Finally we investigate the spatial distribution of jerk activity around global events in figure 3.14, which shows the value of Δ with largest absolute value in the

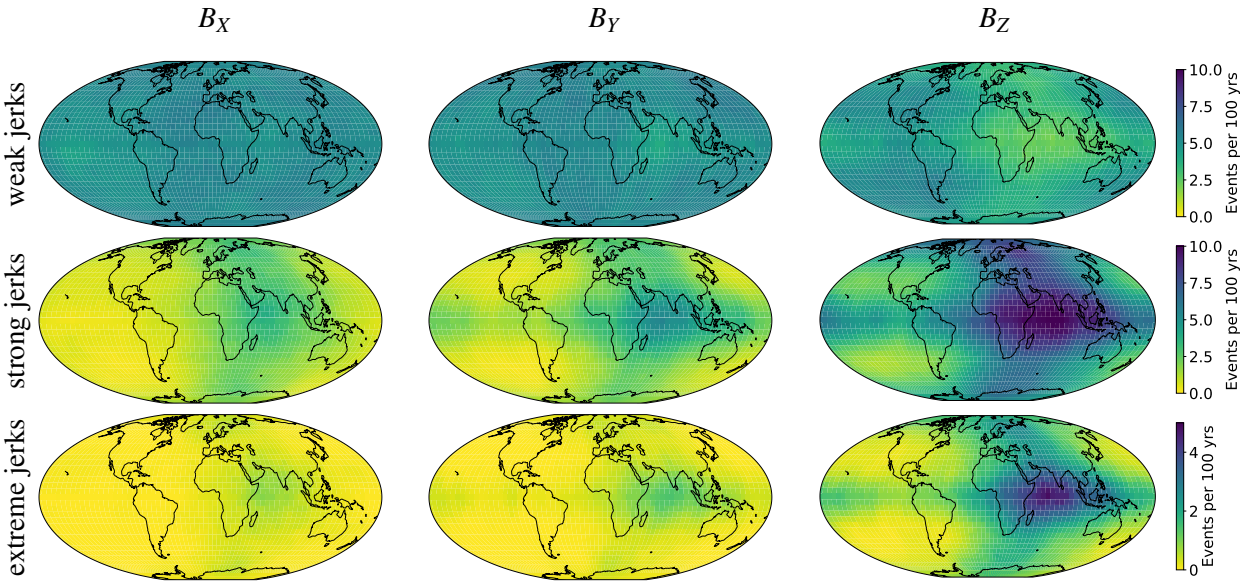

Figure 3.13: Frequency of weak jerks ($|\Delta| < 5$ nT/yr^2, upper row), strong jerks ($5 < |\Delta| < 10$nT/yr^2, middle row) and extreme jerks ($10 < |\Delta| < 50$nT/yr^2, bottom row) for each component X, Y and Z. Weak jerks have a homogeneous distribution, but in this model strong and extreme jerks are centred around the Indian ocean.

10 year time interval centred on four global events. The four global events (from the catalogue) that have been chosen are 1, 5, 8 and 9, which correspond to shallow wave, deep wave, shallow convection and shallow wave triggering respectively. The left column shows the signature in B_Y, which should be compared to figure 12 of Aubert et al (2022). The right column shows the signature in B_Z, which is more pronounced than that in B_Y. None of the jerk events are global, as there are patches of white in all the figures (corresponding to locations where there were no jerks). Jerk 9 has the highest value of $|\Delta|$ yet jerk 5 and 8 are more global. The events driven by wave breaking have high equatorial symmetry, whereas that caused by convection (event 8) is focussed at high southern latitude. This lack of symmetry is much more apparent in figure 3.14 than in the equivalent plot of Aubert et al (2022). The equatorial symmetry of a jerk may therefore be a useful discriminant for the triggering mechanism: non-equatorial signatures are non-wave triggered.

Comparison to the Earth

It is of interest to relate the results from the 71% path model to Earth. The path model is designed so that the timescales and amplitudes of SV and SA are Earth-like; however, at 71% of the path not all rapid dynamics are resolved and as we approach 100% of the path, we would expect jerks of higher amplitude for any given recurrence time. Following Aubert and Gillet (2021); Aubert (2023) we

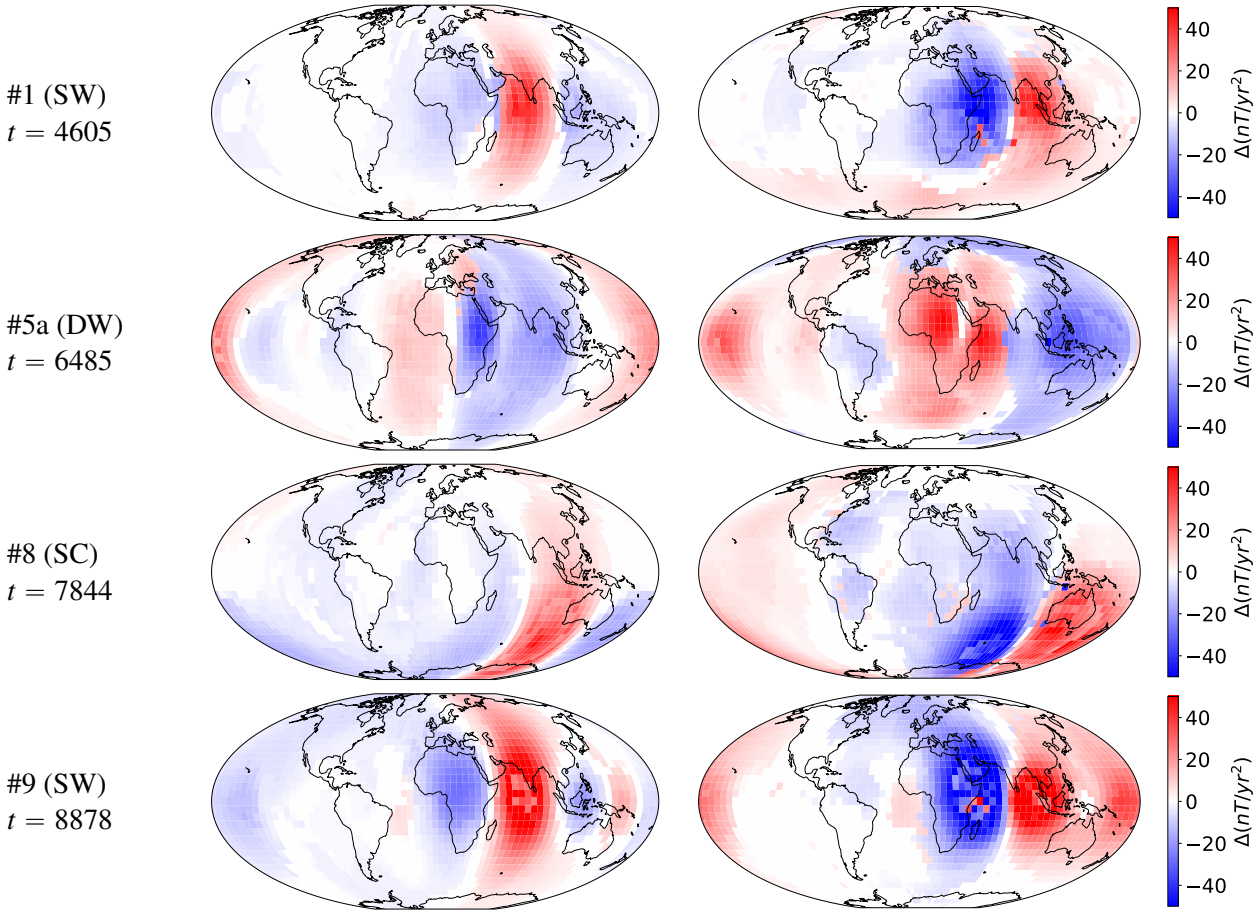

Figure 3.14: Spatial distribution of Δ which has the maximum absolute value in the 10yr time interval centred on the reported global jerk event time, for events 1,5,8,9 in rows 1-4. The left column shows the signal in B_Y, and the right column the signal in B_Z.

therefore transform figure 3.9 showing the recurrence time of jerks, increasing all the jerk strengths by a factor of $\sqrt{100^{1/4}} \approx 1.8$ (noting that E_J scales with the path parameter ϵ as $\epsilon^{-1/4}$, and Δ scales like $\sqrt{E_J}$. Figure 3.15 shows the Earth-like recurrence time for jerks in the three components. In the satellite era, the jerk amplitude for the 2003 jerk in the Z component was about 30 nT/yr^2 (e.g. Olsen and Mandea, 2007), which corresponds to a recurrence time of about 5 years. Thus the rescaled numerical model appears to be consistent with the geomagnetic field. Interestingly, this also means over the course of an average 20 year time period, we would expect to see one double-strength jerk with amplitude 60 nT/yr^2 in the Z-component. There is no evidence to suggest we have seen such an event in the era of continuous satellite monitoring (1999-).

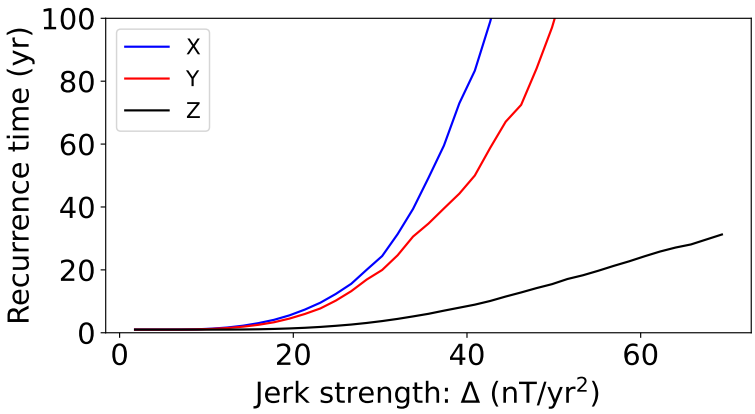

Figure 3.15: Recurrence time of jerk events with $|\Delta|^{max}$ exceeding a given threshold anywhere on Earth's surface, for each component. Rescaled to Earth, i.e. 100% path.

Conclusions

Overall, this report has documented the application of a new Bayesian local jerk-finding method to the 10000 year dataset of the 71% path geodynamo model. Key findings are:

- The jerk-finding tool can rediscover jerks reported in the literature found using other techniques, but using an automated approach based on a piecewise linear representation.
- We rediscover the 14 global jerks reported by Aubert et al (2022), while documenting many more local events.
- Jerks in the different magnetic components often occur with a short time delay (1-2 years).

- Jerks in the Z-component are much more common and stronger than in the other components.
- There are no quiet times for jerks: every year there is at least one jerk (somewhere).
- Weak events occur everywhere with uniform frequency, while stronger events are focussed around the Indian ocean.
- Equatorial symmetry of jerk signatures could be a useful discriminant between different triggering mechanisms.
- Recurrence times, rescaled to Earth, indicate that jerks in the Z-component with amplitude 30 nT/yr^2 occur every 5 years, whereas events twice as strong occur every 20 years.

acknowledgements

Numerical computations were performed on the S-CAPAD/DANTE platform, IPGP, France.

data availability

Python code that implements this methodology can be found at

`https://github.com/plivermore/jerk_finder`

Bibliography

Alexandrescu M, Gibert D, Hulot G, Le Mouël JL, Saracco G (1995) Detection of geomagnetic jerks using wavelet analysis. Journal of Geophysical Research: Solid Earth 100(B7):12,557–12,572

Aubert J (2023) State and evolution of the geodynamo from numerical models reaching the physical conditions of earth's core. GJI 235(1):468–487

Aubert J, Finlay CC (2019) Geomagnetic jerks and rapid hydromagnetic waves focusing at earth's core surface. Nature Geoscience 12(5):393–398

Aubert J, Gillet N (2021) The interplay of fast waves and slow convection in geodynamo simulations nearing earth's core conditions. GJI 225(3):1854–1873

Aubert J, Finlay CC, Fournier A (2013) Bottom-up control of geomagnetic secular variation by the Earth's inner core. Nature 502:219–223

Aubert J, Livermore PW, Finlay CC, Fournier A, Gillet N (2022) A taxonomy of simulated geomagnetic jerks. GJI 231(1):650–672

Backus G, Parker R, Constable C (1996) Foundations of Geomagnetism. CUP

Blangsbøll RM, Finlay CC, Kloss C (2022) Localized origin at the core-mantle boundary of the 1969 geomagnetic impulse. Geophysical Research Letters 49(23):e2022GL101,070

Bodin T, Sambridge M, Rawlinson N, Arroucau P (2012) Transdimensional tomography with unknown data noise. Geophys J Int 189(3):1536–1556

Brown W, Mound JE, Livermore PW (2013) Jerks abound: An analysis of geomagnetic observatory data from 1957 to 2008. Phys Earth Planet Int 223:62–76

Finlay CC, Kloss C, Olsen N, Hammer MD, Tøffner-Clausen L, Grayver A, Kuvshinov A (2020) The CHAOS-7 geomagnetic field model and observed changes in the South Atlantic Anomaly. Earth, Planets and Space 72(1):1–31

Hellio G, Gillet N, Bouligand C, Jault D (2014) Stochastic modelling of regional archaeomagnetic series. Geophys J Int 199(2):931–943

Huder L, Gillet N, Finlay CC, Hammer MD, Tchoungui H (2020) Cov-obs. x2: 180 years of geomagnetic field evolution from ground-based and satellite observations. Earth, Planets and Space 72(1):1–18

Jaynes ET (2003) Probability theory: The logic of science. Cambridge university press

Livermore PW, Fournier A, Gallet Y, Bodin T (2018) Transdimensional inference of archeomagnetic intensity change. Geophys J Int 215(3):2008–2034

Mandea M, Holme R, Pais A, Pinheiro K, Jackson A, Verbanac G (2010) Geomagnetic jerks: rapid core field variations and core dynamics. Space science reviews 155(1):147–175

Olsen N, Mandea M (2007) Will the magnetic North Pole move to Siberia? Eos, Transactions American Geophysical Union 88(29):293–293

Pavón-Carrasco FJ, Marsal S, Campuzano SA, Torta JM (2021) Signs of a new geomagnetic jerk between 2019 and 2020 from Swarm and observatory data. Earth, Planets and Space 73(1):1–11

Pinheiro K, Jackson A, Finlay C (2011) Measurements and uncertainties of the occurrence time of the 1969, 1978, 1991, and 1999 geomagnetic jerks. Geochemistry, Geophysics, Geosystems 12(10)

Roberts GO (1996) Markov chain concepts related to sampling algorithms. in Markov chain Monte Carlo in practice pp 45–57

Sambridge M, Gallagher K, Jackson A, Rickwood P (2006) Trans-dimensional inverse problems, model comparison and the evidence. Geophys J Int 167(2):528–542

3.2 An ensemble of 3D base states for Earth's core dynamics at epoch 2000 determined by geomagnetic data assimilation in a numerical geodynamo model

4DEarth_Swarm_Core ESA project deliverable CCN1 R-O.1

J. AUBERT
IPG PARIS

This deliverable is contained in the following publication: J. Aubert, State and evolution of the geodynamo from numerical models reaching the physical conditions of Earth's core, *Geophys. J. Int.*, 235(1), 468-487.

abstract:

Our understanding of the geodynamo has recently progressed thanks to geomagnetic data of improved quality, and analyses resting on numerical simulations of increasing realism. Here, these two advances are combined in order to diagnose the state and present dynamics of Earth's core in physically realistic conditions. A sequential, ensemble-based framework assimilates the output of geomagnetic field models covering the past 180 yr into a numerical geodynamo simulation, the physical realism of which is also advanced as data is assimilated. The internal dynamical structure estimated for the geodynamo at present reproduces previously widely documented features such as a planetary-scale, eccentric westwards gyre and localization of buoyancy release beneath the Eastern (0°E – 180°E) hemisphere. Relating the typical magnetic variation timescale of the assimilated states to the power at which they operate, the present convective power of the geodynamo is estimated at 2.95 ± 0.2 TW, corresponding to an adiabatic heat flow out of the core of 14.8 ± 1 TW if the top of the core is convectively neutrally stratified at present. For the first time, morphologically and dynamically relevant trajectories are obtained by integrating the estimated states forward for a few decades of physical time using a model reaching the physical conditions of Earth's core. Such simulations accurately account for the spatio-temporal content of high-resolution satellite geomagnetic field models and confirm earlier interpretations in terms of rapid core dynamics. The enforcement of a realistic force balance approaching a Taylor state allows for propagation of weak (velocity perturbation of about 0.6 km.yr^{fl1}) axisymmetric torsional waves with period about 5 yr, supported by a magnetic field of root-mean-squared amplitude of 5.6 mT inside the core. Quasi-geostrophic magneto-Coriolis waves of interannual periods and significantly stronger velocity perturbation (about 7 km.yr^{fl1}) are also reproduced, with properties that converge towards those recently retrieved from the analysis of geomagnetic variations before fully achieving Earth's core conditions. The power spectral density of mag-

netic variations falls off rapidly at frequencies exceeding the inverse Alfvén time (about 0.6 yr^{fl1}), which indicates that the excitation of hydromagnetic waves occurs preferentially at large spatial scales. The possibility to account for geomagnetic variations from years to centuries in physically realistic models opens the perspective of better constraining properties of the deep Earth through geomagnetic data assimilation.